



TU Clausthal

Clausthal University of Technology

Parameter identification of the passive response in arteries

**Rose Rogin Gilbert, Stefan Hartmann,
Laszlo Kudela, Ernst Rank, Gideon Sahar,
Zohar Yosibash, Ofry Yossef**

Technical Report Series

Fac3-16-01



Faculty of
Mathematics/Computer Science
and Mechanical Engineering
Clausthal University of Technology

Impressum

Publisher: Fakultät für Mathematik/Informatik und Maschinenbau,
Technische Universität Clausthal
Am Regenbogen 15, 38678 Clausthal-Zellerfeld, Germany

Editor-in-chief: Alfons Esderts

Technical editor: Volker Wesling

Contact: martina.waechter@tu-clausthal.de

URL: <http://www.fakultaet3.tu-clausthal.de/forschung/technical-reports/>

ISSN: 1869-8018

The Faculty of Mathematics/Computer Science and Mechanical Engineering Review Board

Prof. Dr. Frank Endres

Prof. Dr. Alfons Esderts

Prof. Dr. Stefan Hartmann

Prof. Dr. Olaf Ippisch

apl. Prof. Dr. Günter Kemnitz

Prof. Dr. Armin Lohrengel

Prof. Dr. Norbert Müller

Prof. Dr. Christian Rembe

Prof. Dr. Hubert Schwarze

Prof. Dr. Volker Wesling

Parameter identification of the passive response in arteries

Rose Rogin Gilbert, Stefan Hartmann, Laszlo Kudela, Ernst Rank, Gideon Sahar, Zohar Yosibash, Ofry Yossef

Institute of Applied Mechanics, Clausthal University of Technology, Clausthal-Zellerfeld, Germany
Computation in Engineering, Technische Universität München, Munich, Germany
Soroka Medical Center, Ben-Gurion University of the Negev, Beer-Sheva, Israel
Lab of Computational Mechanics, Ben-Gurion University of the Negev, Beer-Sheva, Israel

Abstract

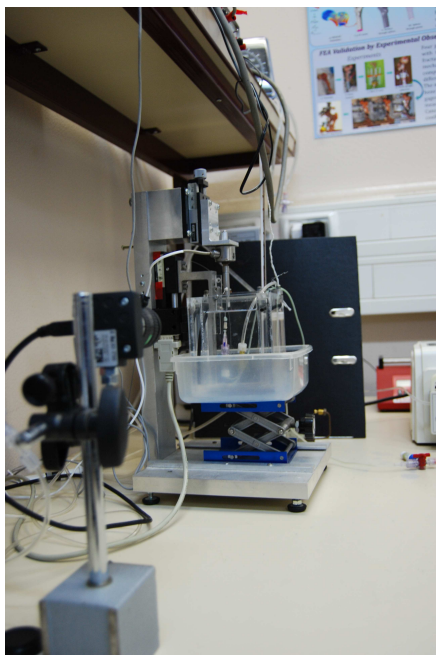
This article discusses the passive response of arteries, with a particular focus on the material parameter identification process of constitutive model of anisotropic hyperelasticity. The arterial wall is composed of three layers: tunica intima, tunica media and tunica adventitia. However, only the media and the adventitia are assumed to be mechanically relevant tissue layers. Thus, it is necessary to determine a set of material parameters for each contributing layer, based on inhomogeneous stress-strain state in an experimental setup. In these tests, tensile and internal pressure loading paths are applied on a human mammary artery, which is embedded in a tank filled with Krebs solution. The artery was proved, in previous works, to be slightly compressible and anisotropic. We draw on the model of Nolan et al. (2014) to identify the material parameters, based on the experimental data provided by contour lines and using digital imaging analysis. The experimental protocol is explained in detail. From the experiments, the axial reaction force and displacement in the radial direction are used to determine the material parameters by using finite element simulations. A particular focus lies on the highly correlated solution between material parameters in the layer, emphasizing the extreme difficulties of a “unique” identification.

1 Introduction

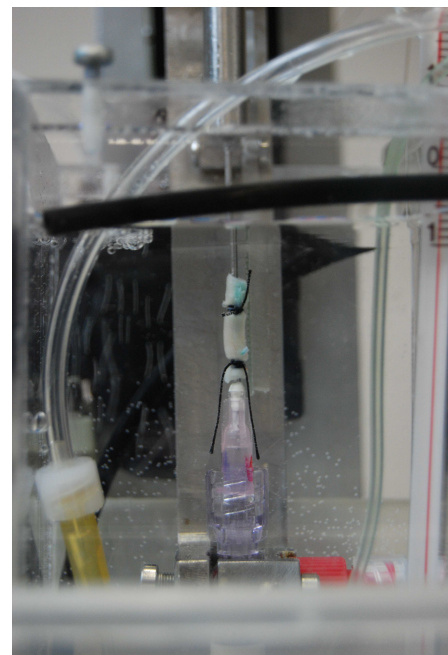
The constitutive modeling of human arteries is an important and challenging topic in biomechanics. A reliable model that may accurately predict the passive and active response of arteries may have a significant influence on the outcome of surgeries. It is also useful for diagnostic and treatment purposes, see (Dumoulin and Cochelin, 2000; Gourisankaran and Sharma, 2000; Gasser and Holzapfel, 2007; Wu et al., 2007). Ottensmeyer et al. (2004) showed that constitutive modeling of arteries may also help to distinguish between healthy and diseased tissue. The mechanical properties of arterial walls are different in circumferential and axial directions due to anisotropy as explained by Rhodin (2011). For this reason, uniaxial tests alone are inconclusive. The number of experimental studies to understand the passive response of arteries are less when compared to the number of studies performed to develop constitutive models. Biaxial and planar tests were performed on arteries of different animals like rats, dogs, and porcine to understand the passive response of arteries, see (Chuong and Fung, 1983; von Maltzahn et al., 1984; Guccione et al., 1991; L'italien et al., 1994; Sacks, 2000; Criscione et al., 2003a,b; Sun et al., 2003; Lu et al., 2005). Planar biaxial stretching and uniaxial tension tests were performed on dilated human ascending aorta by Okamoto et al. (2002) to understand the mechanical properties. Most of the experiments were done using either cruciform or square samples, see (Virues Delgado et al., 2006). Experiments were also performed to determine the shear modulus of the blood vessel wall, see (Deng et al., 1994).

In our investigation, a small length of human internal mammary artery is used to perform tension-inflation experiments to model the passive response of arteries. We chose internal mammary arteries (left and right) as they are very frequently used in bypass-surgeries - which is why their mechanical response under varying loads is of particular interest. The real in-vivo loading conditions (internal pressure, axial stretch) are not well-known. Thus, different loading paths are used to investigate the basic mechanical behavior. The arteries are provided by the Soroka Medical Center, Israel, and the length of the artery depends on the availability after completion of surgery.

A special testing device was developed for the sake of applying axial displacements and internal pressure, and to measure both the axial force using a force device as well as the radial deformation by means of digital images. For a typical setup see Fig. 1(a), where a mammary artery is fixed to two needles in a Krebs solution at $37 \pm 2^\circ\text{C}$



(a) Digital camera and experimental setup



(b) Artery in Krebs-solution

Figure 1: Experimental setup

(body temperature). Obviously, it is not possible to assess the local material behavior directly, as it would be wrong to assume a specified local deformation. Moreover, the heterogeneity of the specimens, their particular internal structure, and their varying geometry counteract to the goal of obtaining a local material property. Thus, the results of the experiments must be interpreted as a structural behavior in a more general sense.

Although the active response, see works of (Hollander et al., 2011; Schmitz and Böl, 2011; Stålhand et al., 2011; Böl et al., 2012; Yosibash and Priel, 2012; Chen et al., 2013), is of particular interest, the passive response has to be investigated first in order to develop an appropriate constitutive (mathematical) model. There are a huge number of papers discussing the modeling of passive response of arteries. Fung et al. (1979) based the formulation on two-dimensional exponential function rather than using a strain-energy function of polynomial type, as proposed by Vaishnav et al. (1973). Chuong and Fung (1983) introduced a three-dimensional model of exponential type, enforcing incompressibility (using undetermined pressure p). Fung et al. (1979) proposed models based on the global observations of tissue behavior rather than mechanical behavior of individual layers. In their respective works, von Maltzahn et al. (1984) as well as Takamizawa and Hayashi (1987) also reported that exponential functions as proposed by Fung et al. (1979) describe the passive response of the artery better than the polynomial function. For carotid arteries however, Takamizawa and Hayashi (1987) suggested that a logarithmic form of strain-energy function can provide a better description of the behavior than Fung's type. They considered incompressibility by using the undetermined pressure p . Delfino et al. (1997) proposed a model taking into account the varying thickness of the arterial wall along the bifurcation. The material was considered to be hyperelastic, incompressible, homogeneous, and isotropic. Generally, in the case of fiber-reinforced materials, the strain-energy can be assumed to contain both the contribution from the fiber as well as the ground substance. In accordance with this formulation, Weiss et al. (1996) proposed a constitutive model where a new parameter was introduced to account for the anisotropic contribution. The Mooney-Rivlin model, (Rivlin and Saunders, 1951), was used to describe the ground substance. Nowadays, very often the hyperelastic constitutive model proposed by Holzapfel et al. (2000) is used for the simulation of soft tissues in the scope of modeling collagen fibers. This work is based on the previously published work of Weiss et al. (1996) and was extended to the inelastic domain, see the works of Gasser and Holzapfel (2002) and Holzapfel et al. (2002).

The property of polyconvexity ensures the existence of a solution for a boundary value problem. Schröder and Neff (2001) first extended polyconvexity to anisotropy. A new class of isotropic hyperelasticity relations for nearly-incompressible materials based on principal invariants was proposed by Hartmann and Neff (2003). The issue of coerciveness was addressed in that paper as well. Schröder and Neff (2003) proposed a polyconvex anisotropic hyperelastic function within the framework of invariant theory. Proof of a variety of isotropic and transversely isotropic functions can be found in that paper. Itskov et al. (2006) proposed a new class of anisotropic (orthotropic and transversely isotropic) polyconvex strain-energy functions represented by a series with an arbitrary number of terms - each term of the series satisfying a priori the condition of the energy- and stress-free natural state. The main drawbacks of the models proposed by Schröder and Neff (2003) and Itskov et al. (2006) are the large number of material parameters necessary to characterize the material behavior. Schröder and Neff (2002) proposed a polyconvex free energy for soft tissues, based on (Schröder and Neff, 2001) and (Schröder and Neff, 2003). They assumed the tissues to be transversely isotropic. Balzani et al. (2006) put forward a new form of polyconvex stored energies to represent the behavior of soft biological tissue. The main advantage was the limited number of parameters to represent the stress-strain curves. Zdunek et al. (2014) use a clear decomposition into volume preserving and volume changing as well as compressible and isochoric, to provide a new framework for nearly incompressible and strongly transversely isotropic finite hyperelasticity.

Many authors assume the artery to be slightly compressible, see works of (Iannaccone et al., 2014; Cardoso et al., 2014). In our study, we consider the artery to be compressible as well - based on the investigations of Yosibash et al. (2014), where the compressibility of the arteries has been experimentally proven. Nolan et al. (2014) proposed the usage of a 'total' right Cauchy-Green tensor in the anisotropic strain-energy function at specific places rather than an unimodular right Cauchy-Green tensor. In our work, the model of Nolan et al. (2014) is used to model the anisotropic behavior of both the media and the adventitia. The model was implemented into the finite program TASAFEM. The artery is modeled as a two layered specimen consisting of media and adventitia, and the angles of the helix in the two layers are assumed to differ. The model is then fitted to the experimental results to identify the material parameters of the media and the adventitia.

The identification of the material parameters is a very important issue in constitutive modeling. Sufficient experimental data are necessary to identify the material parameters. Most of the previous studies were conducted based on cruciform or square samples and by using the force-length measurements on animal arteries. Previous works were based on assumptions like axisymmetry and/or a single homogeneous layer, see the works by (Holzapfel et al., 2005; Gleason et al., 2008; Ning et al., 2010). A study conducted by Sutton et al. (2008) was based on a 3D-Digital Image Correlation (DIC) stereo-microscopy system on the carotid artery of a mouse. Badel et al. (2012) performed a simultaneous inverse identification of material parameters in both media and adventitia using DIC-surface strain measurements. In that work, a highly contrast speckle pattern was applied on the arterial wall using ethidium bromide nuclear staining for the purpose of image processing. They concluded that the

experimental data from two different layers would be more accurate than data averaged over the wall (assuming the wall to be a single homogeneous layer).

In the scope of our investigations, we are interested in the questions how we can obtain the material parameters using information of digital images and how reliable material parameter identification can be today. Since the geometry of real arteries is highly curvilinear, the material is layered and each layer behaves anisotropic, the artery's response has to be modeled by means of finite elements. In other words, in a first step, the geometrical data of the artery has to be determined. The numerical results of the finite element computations have to be compared to the experimental results in a least square sense. These ideas go back to Mahnken and Stein (1996), Kreißig (1998), Scheday (2003), Hartmann et al. (2003), and the references cited therein. We follow this concept, but extend the investigations to measures representing the quality of the identification process. The experiments are performed to obtain the axial reaction force and the radial displacements for given axial displacements and internal pressure. Based on the idea proposed by Hartmann et al. (2003), the digital images are taken using high resolution camera, and the radial displacements are determined from the image with the help of a contour detection tool. A trust-region reflective algorithm, provided in Matlab, is used to find the best-fit parameters in a least-square sense, and a data optimization tool was developed which calls the finite element program during each iteration of the optimizer. The correlation between the set of parameters assigned to each layers is studied to better understand the reliability of the material parameter identification. Additionally, measures representing the quality of the identification are investigated to discuss the reliability, see (Krämer et al., 2015).

The structure of the paper is as follows. Section 2 summarizes the histology of the artery. We discuss each layer and point out the importance of the media and the adventitia. Section 3 serves to explain the experimental protocol and the analysis of experiment, including details on the particular loading processes of the experiment. The data from the experiments are analyzed as well. Section 4 summarizes the constitutive model that is used to define the passive response of the artery. Subsequently, the methodology involved in material parameter identification and the application of the procedure to the experimental data are provided in Section 5. The results are discussed in Section 6. Finally, some concluding remarks and outlook are discussed.

In this paper, upper-case, bold-faced letters, for example \mathbf{C} , represent second order tensors and lower-case letters with an arrow on the top symbolize geometrical vectors, for example \vec{a} . \mathbf{A} represents a matrix, whereas \mathbf{a} defines column vectors.

2 Histology of the Artery

According to Rhodin (2011), the most general classification of arteries is to distinguish elastic and muscular tissues. Elastic arteries are those with large diameter consisting of smooth muscle cells as well as elastic laminae. Arteries that decrease in diameter as they approach the periphery of the organs - and that mainly consist of smooth muscle cells with less elastic laminae - are known as muscular arteries. The arterial wall is composed of three distinct layers: *tunica intima*, *tunica media* and *tunica adventitia*. The intimal layer is the innermost layer and is made up of endothelial cells. In most arteries, the media is composed mainly of smooth muscle cells (SMC) making the media responsible for the active response of the arteries. The adventitia is the outermost layer. The wavy collagen fibrils that can be found in this layer are arranged in helical structures, preventing damages to the artery. For a more detailed explanation on the histology of the artery, see the works of (Rhodin, 2011); see Fig. 2 as well.

2.1 Intima

The tunica intima is the innermost layer of an artery. It consists of the endothelium, an internal elastic membrane and subendothelial connective tissue composed of collagenous bundles, elastic fibrils and some smooth muscle cells. However, the subendothelial layer is found only in large elastic arteries such as the aorta. It is absent in other elastic arteries such as carotid and mammary arteries. The endothelial cells provide a physical barrier between the blood and the subendothelial tissue. Gender, age, and disease determine the thickness of the subendothelial layer. The intima becomes thicker and stiffens with growing age (known as arteriosclerosis) which is why the mechanical contribution might be a significant aspect. Mostly, however, the intima is very thin - which is why the mechanical contribution of the intima is considered to be insignificant and hence neglected.

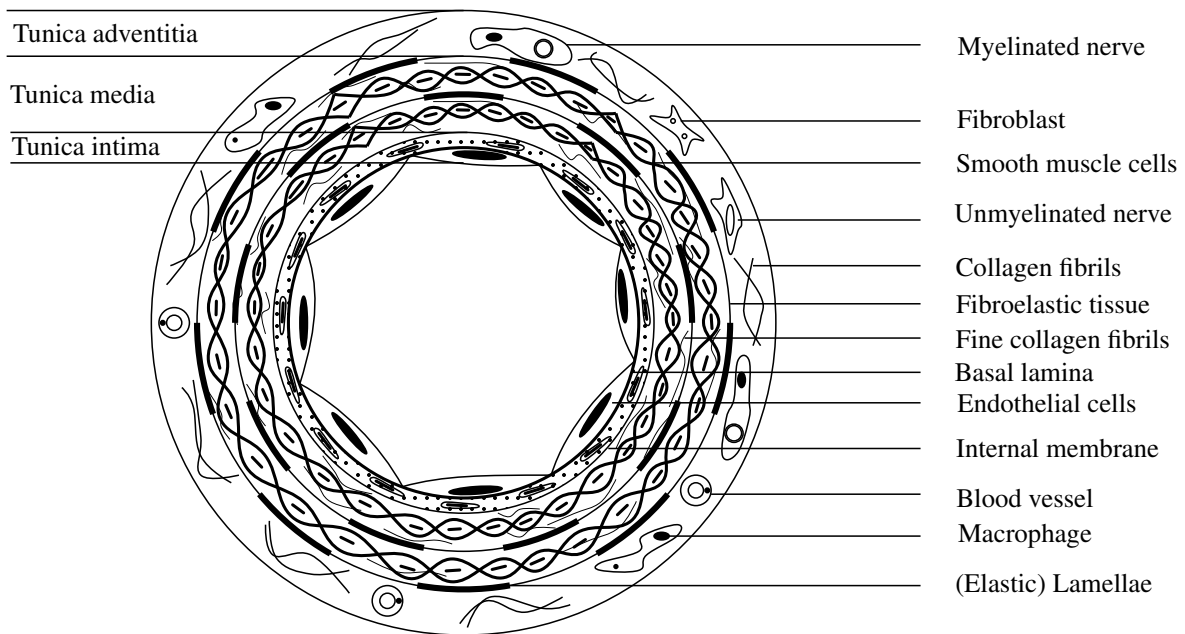


Figure 2: Cross section of an artery (based on Rhodin (2011))

2.2 Media

From the mechanical point of view, the tunica media is the most important layer in an artery. The media, as the name suggests, is the middle layer of the artery and is separated from the intima and the adventitia by internal and external elastic laminae. The media is composed of the following:

- **Elastin:** it can be found in the form of fenestrated sheets or lamellae arranged in concentric layers between muscle layers. The amount and thickness of elastin depends on the location of the artery, on the blood pressure, age and gender of the individual. In a male adult, the aorta has 40-70 lamellae. However, at birth the number of lamellae is almost zero.
- **Smooth muscle cells:** similar to elastin the smooth muscle cells (SMC) are also arranged in layers. They are arranged in a low pitch spiral along the axis of the vessel. This helical arrangement results in high strength, resilience and the ability of the media to resist load in axial as well as circumferential direction. The SMC are spindle-shaped cells with elongated nuclei, as depicted in the Fig. 2. The SMC accounts for the active response of the arteries. Hence, the media is responsible for the active response of the arteries.
- **Collagen fibers and ground substance:** they are synthesized and secreted by the smooth muscle cells. They are also arranged in helical structures, which serves to strengthen the arterial wall.

2.3 Adventitia

The tunica adventitia is the outermost layer of the artery and is mainly composed of wavy collagen fibers, fibroblasts and macrophages. It is completely surrounded by connective tissue. The thickness of the adventitia depends mainly on the location of the artery (distance to the heart) and the type of artery (elastic or muscular). Similar to the media, the wavy collagen fibers are also arranged in the form of a helix, giving the artery stability and strength. The collagen fibers help to prevent the expansion of the arterial wall beyond physiological limits during systole of the cardiac cycle. According to the works of von Maltzahn et al. (1984), Yu et al. (1993) and Xie et al. (1995), the media is much stiffer than the adventitia. At higher pressures, however, the wavy collagen fibers straighten up, turning the adventitia into a shield that protects the artery from damages.

3 Experiments on the Mammary Artery

In the following experimental investigation, an internal thoracic artery (commonly called as mammary artery) serves to identify the material parameters. Usually, a cardiac surgeon will prefer a mammary artery over saphenous vein grafts or other arteries. This is attributed to the long-term patency, improved survival and the resistance of the mammary artery to the development of atherosclerosis, see (Otsuka et al., 2013)

After being extracted during a surgery, the mammary artery is allowed to rest for approximately three hours. Before the mechanical test, the connective tissue surrounding the artery is surgically extracted (this process is known as skeletonization). Then, it is fixed to a testing device. For a typical setup see Fig. 1(a), where the mammary artery is fixed to two needles in a Krebs solution at $37 \pm 2^\circ\text{C}$ (body temperature). The camera used to obtain the digital images in order to determine the radial displacements is IDS USB UI-1485LE with a CMOS sensor in 5 megapixel resolution. The images are taken at a framing rate of 2 fps. Using the experimental apparatus, the maximum displacement that can be measured, depends on the length of the artery. In ideal conditions, the maximum is 20mm at a maximum velocity of 0.78m/s. Afterwards, the specimens are pre-conditioned in the following process: ten cycles of axial tension and relaxation (from 0% to 15% of the artery) followed by two cycles of inflation and deflation (20mmHg to 80mmHg).

3.1 Experimental Protocol

After the preconditioning, a complex loading process is applied, which, for the first instance, is not related to physiological conditions. The main goal of the loading and relaxation for a fixed pressure is to identify whether the artery shows viscoelastic properties. Moreover, rate-dependence can be identified if the loading process has a varying loading rate. In the following, two process types are chosen. Firstly, for a constant pressure, cyclic axial displacement loads are chosen. Afterwards, for a constant pre-stretch, we apply a saw tooth-like cyclic pressure load. These subsequently performed loading paths are shown in Fig. 3 - 7.

In addition to an explanation of the experiments, a brief discussion of the chosen units is necessary. In medical applications, the unit mmHg (millimeter of mercury) is chosen, which is not an SI unit. Based on the density of mercury ($\rho = 13595\text{kg/m}^3$) it is the stable pressure of a cube ($1 \times 1 \times 1\text{mm}^3$) upon a surface, $1\text{mmHg} = 133.322365\text{Pa}$. In human arteries, a pressure range under healthy conditions is 80-140 mmHg. In the case of cardiac arrest 6-7 mmHg is observable, whereas 200-220 mmHg is the case for hypertension. The cyclic axial stretch loads indicate pre-stretches which occur in the human body in the regular course of motion, or during bypass surgeries. Cyclic pressure conditions like this are common – although the actual pressure loading paths under real-life conditions are more complicated.

3.1.1 Cyclic Axial Displacements

In the first process, a periodic displacement-controlled load in axial direction of the artery is applied, with a mean-value of the pressure of $p_{\max}^{(1)} = 20\text{mmHg}$. The axial force F is measured by a force gauge. Fig. 3 shows the first 5 cycles (Figs. 4 - 7 are the continuation of the process). The loading- and unloading-rate are chosen to be the same. We choose an amplitude of the stretch $\lambda_{\max}^{(1)} = 1 + (u_{\max}^{(1)}/L_0) = 1.08$, i.e. $u_{\max}^{(1)} = 1.08L_0 - L_0 = 0.08L_0$. The stretch, $\lambda = L/L_0$, is not the local stretch assigned to a material point but the overall stretch between the clamps fixing the artery. Accordingly, L_0 defines the initial length and L the current length. $u = L - L_0$ symbolizes the relative displacement of the two fixed points in the axial direction. After these cycles, the displacement amplitude is increased to $u_{\max}^{(2)} = 1.15L_0 - 1$, where the loading and unloading-rate are the same as in the first cycles. During the next ten cycles, the pressure is increased to a mean-value of $p_{\max}^{(2)} = 40\text{mmHg}$, while the displacement cycles are chosen to be the same as before, see Fig. 4. In a third process, the process is performed again using a pressure mean-value of $p_{\max}^{(3)} = 60\text{mmHg}$, see Fig. 5. The next step is to perform the same axial displacement cycles for a mean pressure of $p_{\max}^{(4)} = 80\text{mmHg}$ as can be seen in Fig. 6. In the final displacement-load, a holding-time of $\Delta t_5 = 3\text{min}$ is introduced to find out whether a relaxation behavior can be observed. The same artery is used for all the experiment steps.

3.1.2 Cyclic Pressure Load

After the axial loading processes, the pressure is varied for a constant axial-displacement of $u_{\max}^{(1)} = 1.08L_0 - 1$ and $u_{\max}^{(2)} = 1.15L_0 - 1$. The maximum pressure is $p_{\max}^{(4)} = 80\text{mmHg}$ and the minimum reads $p_{\max}^{(1)} = 20\text{mmHg}$,

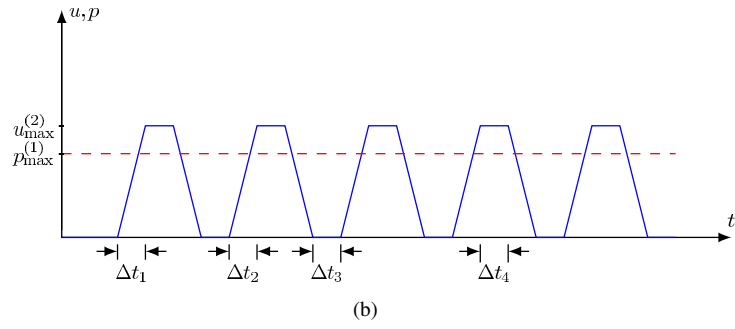
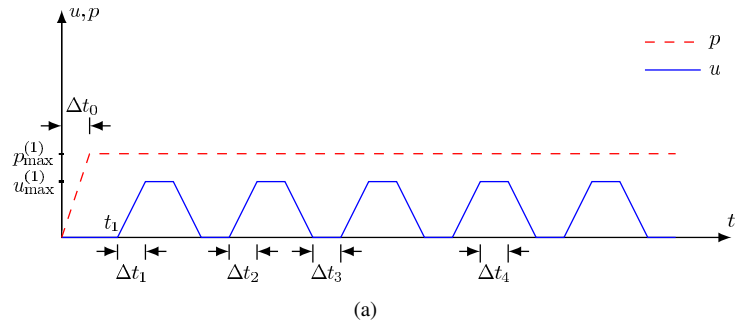


Figure 3: Periodic process with $p_{\max}^{(1)} = 20\text{mmHg}$, ($\Delta t_0 = 5\text{s}$, $t_1 = 10\text{s}$, $\Delta t_1 = 5\text{s}$, $\Delta t_2 = 5\text{s}$, $\Delta t_3 = 5\text{s}$, $\Delta t_4 = 5\text{s}$)

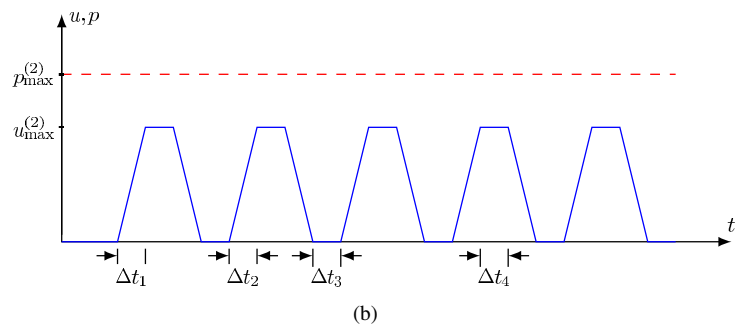
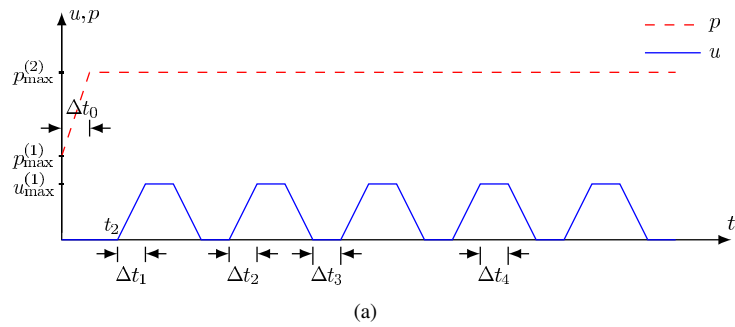


Figure 4: Periodic process with $p_{\max}^{(2)} = 40\text{mmHg}$, ($\Delta t_0 = 5\text{s}$, $t_2 = 10\text{s}$, $\Delta t_1 = 5\text{s}$, $\Delta t_2 = 5\text{s}$, $\Delta t_3 = 5\text{s}$, $\Delta t_4 = 5\text{s}$)

see Fig. 7. The overall experimental process is divided into 11 stages, as shown in Tab. 1.

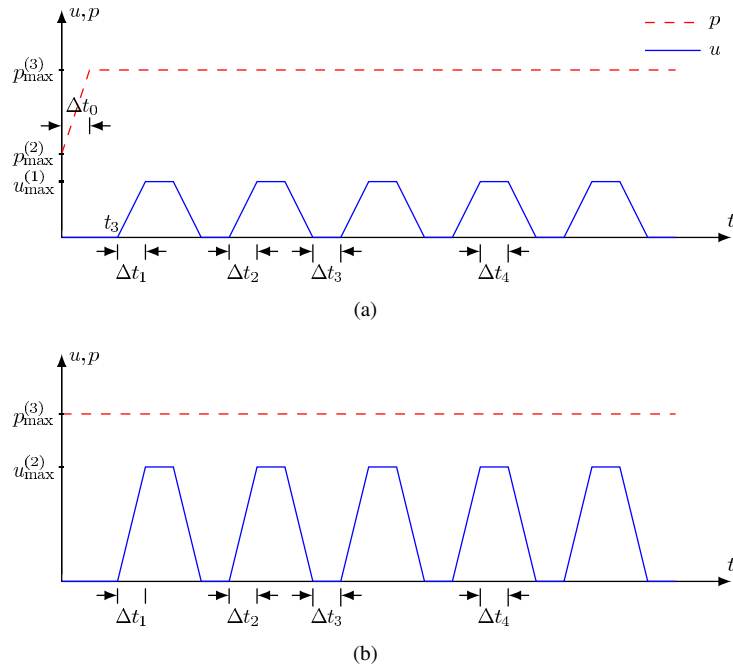


Figure 5: Periodic process with $p_{\max}^{(3)} = 60\text{mmHg}$, ($\Delta t_0 = 5\text{s}$, $t_3 = 10\text{s}$, $\Delta t_1 = 5\text{s}$, $\Delta t_2 = 5\text{s}$, $\Delta t_3 = 5\text{s}$, $\Delta t_4 = 5\text{s}$)

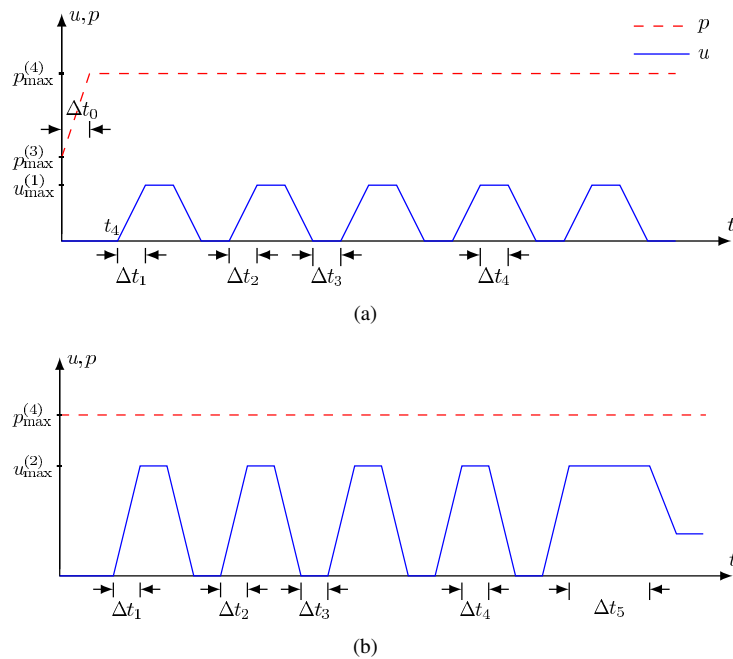


Figure 6: Periodic process with $p_{\max}^{(4)} = 80\text{mmHg}$, ($\Delta t_0 = 5\text{s}$, $t_4 = 10\text{s}$, $\Delta t_1 = 5\text{s}$, $\Delta t_2 = 5\text{s}$, $\Delta t_3 = 5\text{s}$, $\Delta t_4 = 5\text{s}$, $\Delta t_5 = 180\text{s}$)

3.2 Analysis of Experiments

The experiments were conducted according to the protocol mentioned in Tab 1. The entire process of Figs. 3 - 7 are related to results depicted in Figs. 8 - 18. In other words, the process of Fig. 3(a) and Fig. 3(b) is connected to the results of Figs. 8 and 9, and so on. Fig. 8(a) until Fig. 15(a) show that there are pronounced viscoelastic effects in the artery. It can also be seen that the viscoelastic effects are dependent on the axial stretch. The viscoelastic effects

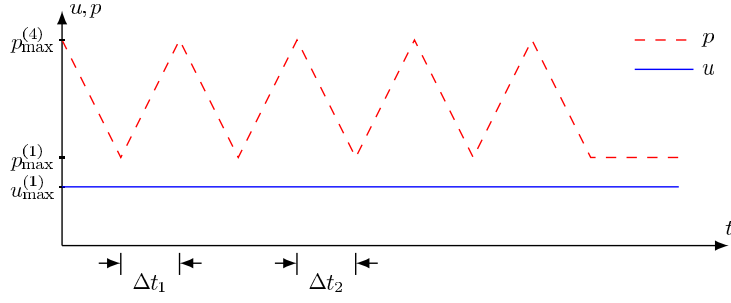


Figure 7: Periodic pressure process with $p_{\max}^{(4)} = 80\text{mmHg}$ and $p_{\max}^{(1)} = 20\text{mmHg}$ as well as $u_{\max}^{(1)} = 1.08L_0 - 1$ and $u_{\max}^{(2)} = 1.15L_0 - 1$, ($\Delta t_1 = 5\text{s}$, $\Delta t_2 = 5\text{s}$)

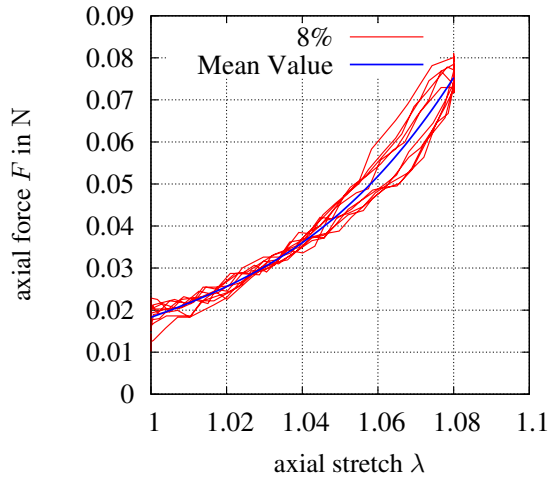
Loading protocol					
stage	axial stretch	axial stretch rate (/s)	pressure (mmHg)	pressure rate (mmHg/s)	no. of cycles / time
1	$1 \leq \lambda \leq 1.08$	0.016	20	0	5 cycles
2	$1 \leq \lambda \leq 1.15$	0.030	20	0	5 cycles
3	$1 \leq \lambda \leq 1.08$	0.016	40	0	5 cycles
4	$1 \leq \lambda \leq 1.15$	0.030	40	0	5 cycles
5	$1 \leq \lambda \leq 1.08$	0.016	60	0	5 cycles
6	$1 \leq \lambda \leq 1.15$	0.030	60	0	5 cycles
7	$1 \leq \lambda \leq 1.08$	0.016	80	0	5 cycles
8	$1 \leq \lambda \leq 1.15$	0.030	80	0	5 cycles
9	$\lambda = 1.15$	0	80	0	3 min
10	$\lambda = 1.08$	0	$10 \leq p \leq 80$	14	5 cycles
11	$\lambda = 1.15$	0	$10 \leq p \leq 80$	14	5 cycles

Table 1: Loading protocol for the experiment

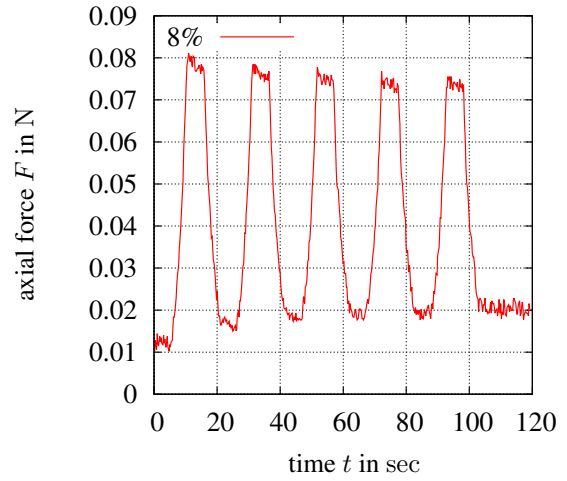
are much more noticeable when the axial stretches are at $\lambda = 1.15$. This can be observed when comparing Fig. 8(a) and Fig. 9(a). The same conclusion can be drawn when further comparisons are made between Fig. 10(a) and Fig. 11(a), Fig. 12(a) and Fig. 13(a), as well as Fig. 14(a) and Fig. 15(a). Fig. 16 clearly illustrates that the artery relaxes when it is kept at constant pressure and constant stretch. Figs. 8(b) and 9(b) indicate that the hold time $\Delta t_4 = 5\text{ sec}$, see Fig. 3, is not enough for reaching the end point of relaxation. In view of constitutive modeling of an overstress-type model, see, for instance, (Haupt, 2001). This is essentially motivated by Fig. 16, which reveals a force relaxation (stress relaxation) of approximately 30%. Certainly, the question arises whether to consider the rate-dependent effects of the modeling of the artery. In the case of critical problems this is necessary. Moreover, hysteretic effects will be observable under physiological conditions. Obviously, the viscous (hysteretic) effects are increasing for larger axial stretches. For the subsequent considerations regarding the parameter identification process, however, the aspect of hysteresis is not considered. From Figs. 17(a) and 18(a), it can be seen that the axial stresses depend on the axial stretch of the artery. The axial stresses are higher if the axial stretch is higher, see Fig. 18(b). According to Agianniotis et al. (2012), the change in axial stresses are negligible with increase in pressure in the physiological range. Thus, it can be concluded that the in-vivo stretch of the artery is between $\lambda = 1.08$ and $\lambda = 1.15$. The change in slope in Figs. 17(a) and 18(a) is the result of the orientation of the fibers in the artery. The response stiffens as the mean orientation approaches the axial direction, see (Gasser et al., 2006; Holzapfel et al., 2015).

4 Constitutive Model

As a first attempt a more or less simple constitutive model of hyperelasticity in the large strain regime has to be chosen to represent the material behavior. Both the media and the adventitia are compressible, see Yosibash et al. (2014). Due to the histological findings regarding the muscle cells or collagen fibers (Rhodin, 2011), the tissue must be anisotropic. Accordingly, we follow the course of modeling and by applying a model of anisotropic

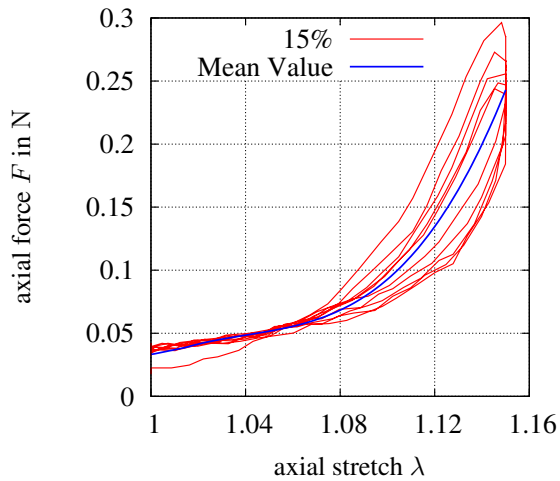


(a) Stage 1: Axial force vs axial displacement

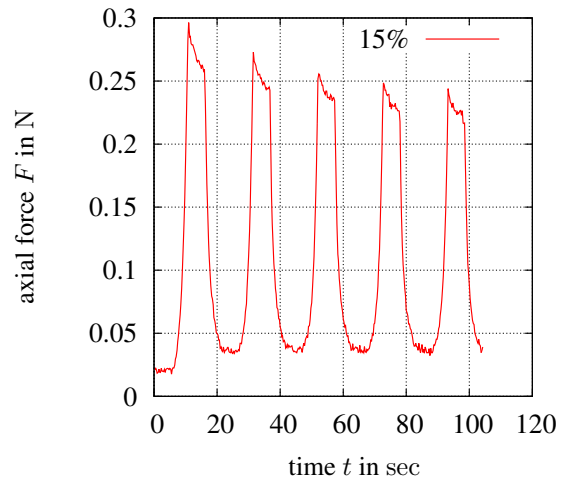


(b) Stage 1: Axial force vs time

Figure 8: Stage 1: pressure = 20mmHg; $\lambda = 1.08$; experiment conducted based on Fig. 3(a)



(a) Stage 2: Axial force vs axial displacement



(b) Stage 2: Axial force vs time

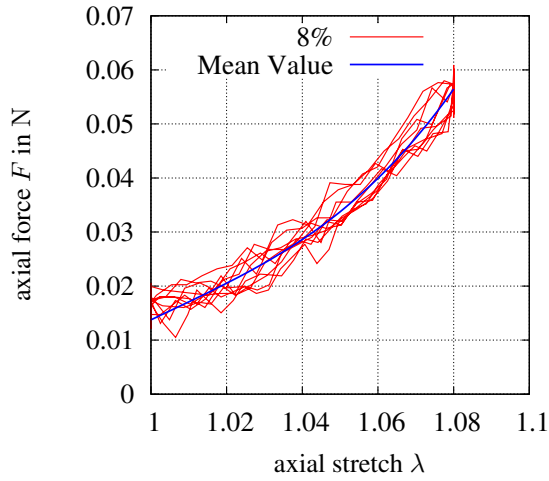
Figure 9: Stage 2: pressure = 20mmHg; $\lambda = 1.15$; experiment conducted based on Fig. 3(b)

hyperelasticity with two fiber directions. They are defined as \vec{a}_0 and \vec{a}_1 , $|\vec{a}_0| = |\vec{a}_1| = 1$, and forming tangent vectors at two helices. These vectors are given by,

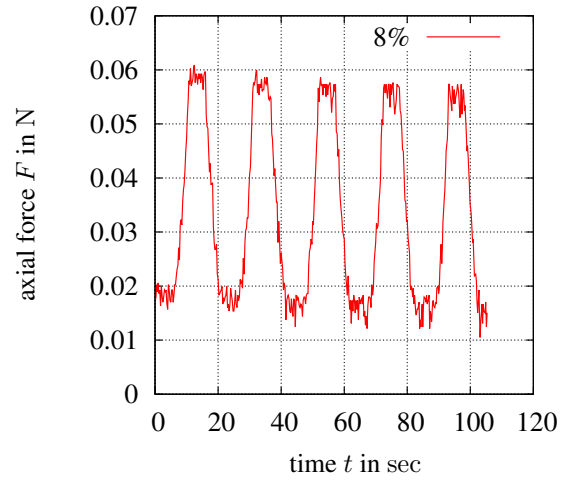
$$\vec{a}_0 = -\cos \beta \frac{Y}{\sqrt{X^2 + Y^2}} \vec{e}_x + \cos \beta \frac{X}{\sqrt{X^2 + Y^2}} \vec{e}_y + \sin \beta \vec{e}_z$$

$$\vec{a}_1 = \cos \beta \frac{X}{\sqrt{X^2 + Y^2}} \vec{e}_x - \cos \beta \frac{Y}{\sqrt{X^2 + Y^2}} \vec{e}_y - \sin \beta \vec{e}_z.$$

The motion of the material body is given by $\vec{x} = \vec{\chi}_R(\vec{X}, t)$, where \vec{X} represents the material placement vector to

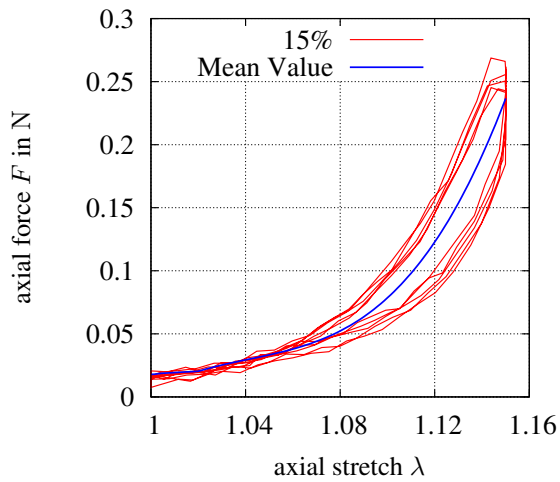


(a) Stage 3: Axial force vs axial displacement

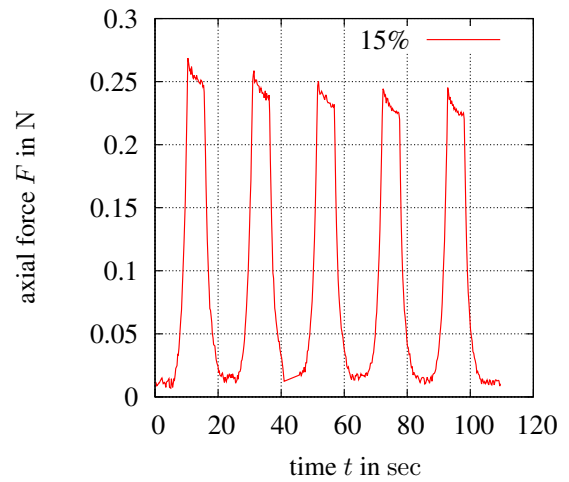


(b) Stage 3: Axial force vs time

Figure 10: Stage 3: pressure = 40mmHg; $\lambda = 1.08$; experiment conducted based on Fig. 4(a)



(a) Stage 4: Axial force vs axial displacement



(b) Stage 4: Axial force vs time

Figure 11: Stage 4: pressure = 40mmHg; $\lambda = 1.15$; experiment conducted based on Fig. 4(b)

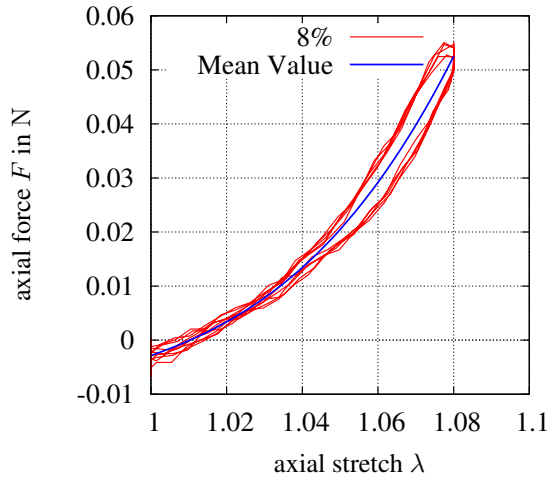
point in the reference configuration and \vec{x} is the current placement of the point at time t . The deformation gradient is defined by $\mathbf{F} = \text{Grad } \vec{\chi}_R(\vec{X}, t)$, indicating the local change of deformation. Commonly, the right Cauchy-Green tensor $\mathbf{C} = \mathbf{F}^T \mathbf{F}$ is chosen. Using the invariants

$$I_1 = \text{tr } \mathbf{C}, \quad I_2 = \frac{1}{2}((\text{tr } \mathbf{C})^2 - \text{tr } \mathbf{C}^2), \quad I_3 = \det \mathbf{C} \quad (2)$$

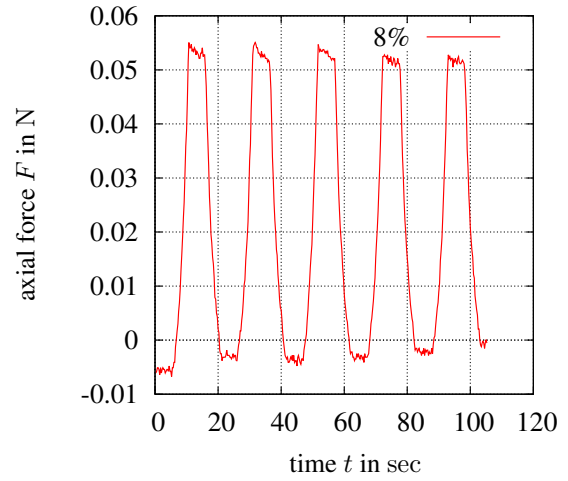
and

$$I_4 = \mathbf{C} \cdot \mathbf{M}_0 = \vec{a}_0 \cdot \mathbf{C} \vec{a}_0, \quad (3a)$$

$$I_6 = \mathbf{C} \cdot \mathbf{M}_1 = \vec{a}_1 \cdot \mathbf{C} \vec{a}_1, \quad (3b)$$

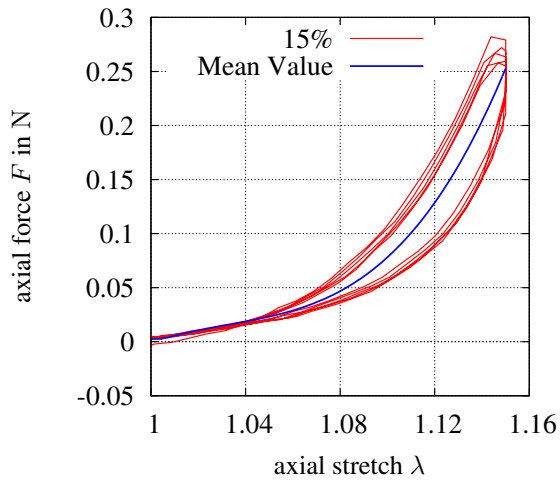


(a) Stage 5: Axial force vs axial displacement

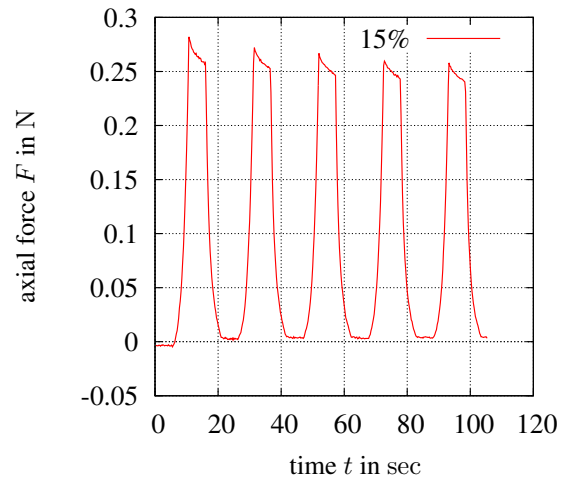


(b) Stage 5: Axial force vs time

Figure 12: Stage 5: pressure = 60mmHg; $\lambda = 1.08$; experiment conducted based on Fig. 5(a)



(a) Stage 6: Axial force vs axial displacement



(b) Stage 6: Axial force vs time

Figure 13: Stage 6: pressure = 60mmHg; $\lambda = 1.15$; experiment conducted based on Fig. 5(b)

the strain-energy function

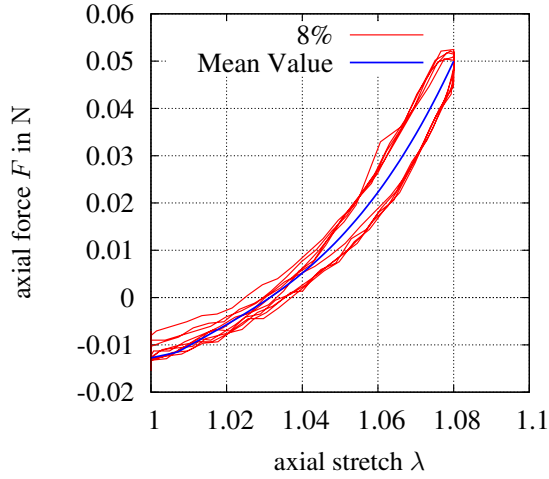
$$\psi(\mathbf{C}, \mathbf{M}_0, \mathbf{M}_1) = \tilde{\psi}(I_1, I_2, I_3, I_4, I_6) \quad (4)$$

with the structural tensors $\mathbf{M}_0 = \vec{a}_0 \otimes \vec{a}_0$ and $\mathbf{M}_1 = \vec{a}_1 \otimes \vec{a}_1$ are defined. As it is common, the strain-energy function is decomposed into an isotropic and anisotropic part

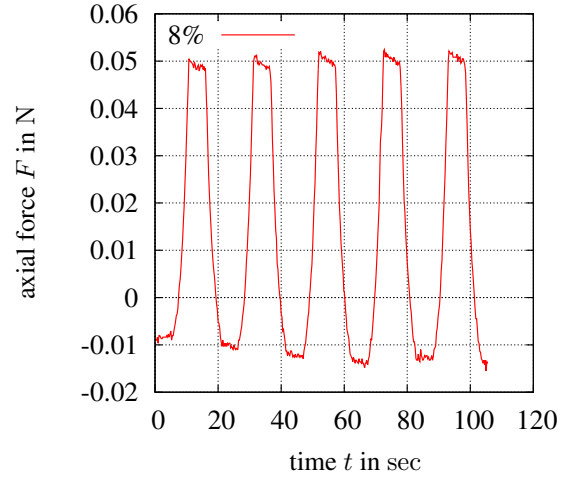
$$\psi(\mathbf{C}, \mathbf{M}_0, \mathbf{M}_1) = \psi_{\text{iso}}(\mathbf{C}) + \psi_{\text{aniso}}(\mathbf{C}, \mathbf{M}_0, \mathbf{M}_1) \quad (5)$$

where the isotropic part is the sum of a volume-changing and a volume-preserving part

$$\psi_{\text{iso}}(J, \bar{\mathbf{C}}) = \psi_{\text{isoch}}(\bar{\mathbf{C}}) + \psi_{\text{vol}}(J). \quad (6)$$

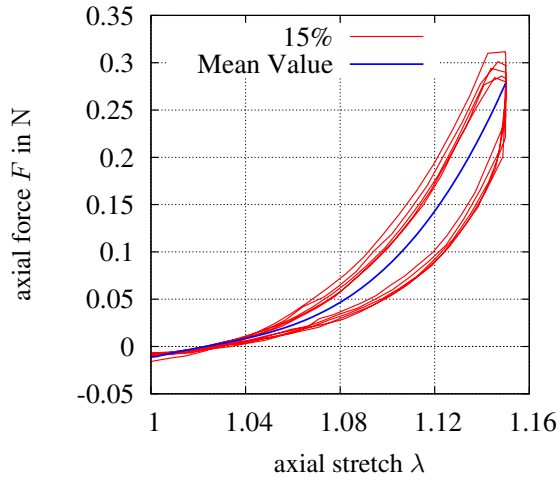


(a) Stage 7: Axial force vs axial displacement

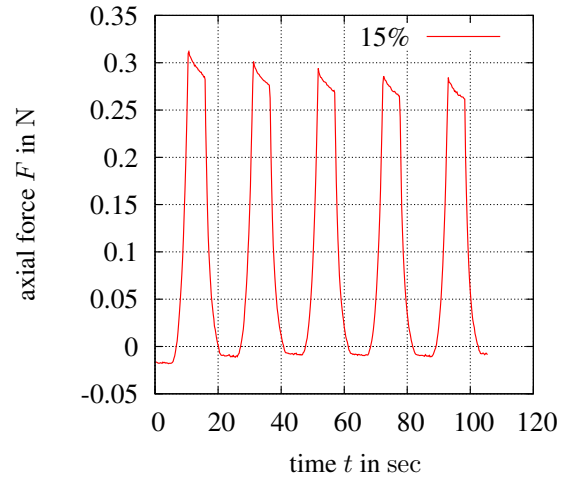


(b) Stage 7: Axial force vs time

Figure 14: Stage 7: pressure = 80mmHg; $\lambda = 1.08$; experiment conducted based on Fig. 6(a)



(a) Stage 8: Axial force vs axial displacement



(b) Stage 8: Axial force vs time

Figure 15: Stage 8: pressure = 80mmHg; $\lambda = 1.15$; experiment conducted based on Fig. 6(b)

The volume-changing part depends on the determinant of the deformation gradient, $J = \det \mathbf{F}$,

$$\psi_{\text{vol}}(J) = \frac{K}{50}(J^5 + J^{-5} - 2) \quad (7)$$

whereas the volume-preserving part depends on the unimodular right Cauchy-Green tensor $\bar{\mathbf{C}} = \bar{\mathbf{F}}^T \bar{\mathbf{F}} = (\det \mathbf{C})^{-1/3} \mathbf{C}$ with $\bar{\mathbf{F}} = (\det \mathbf{F})^{-1/3} \mathbf{F}$ and $\det \bar{\mathbf{F}} = 1$. The simplest model is given by Neo-Hookean model

$$\psi_{\text{isoch}}(I_{\bar{\mathbf{C}}}) = \frac{c_{10}}{2}((\text{tr } \bar{\mathbf{C}}) - 3) \quad (8)$$

with the first invariant $I_{\bar{\mathbf{C}}} = I_1 J^{-2/3}$. With regard to the discussion in (Hartmann and Neff, 2003) the strain energy

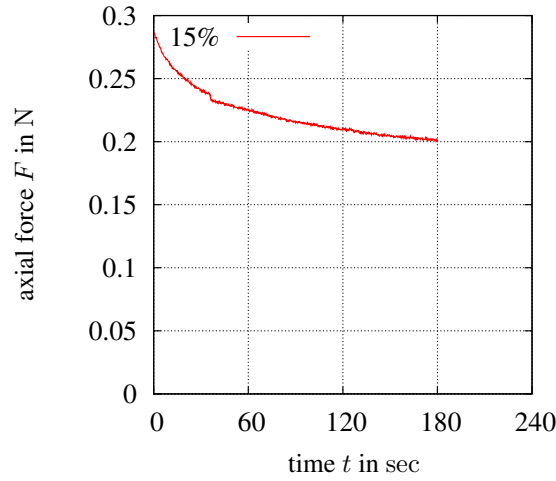
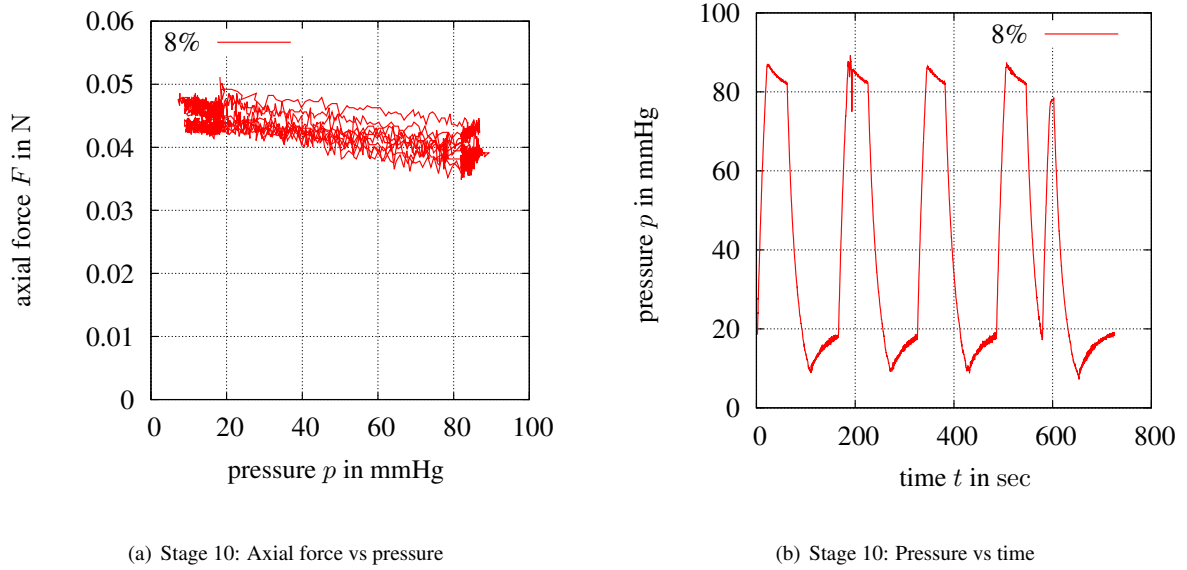


Figure 16: Stage 9: Axial force vs time at pressure = 80mmHg; $\lambda_T = 1.15$; holding time of 3 min



(a) Stage 10: Axial force vs pressure

(b) Stage 10: Pressure vs time

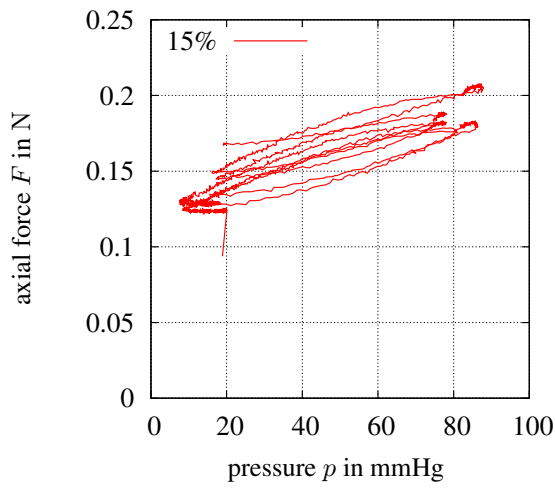
Figure 17: Stage 10: pressure varies from 10 to 80mmHg ; $\lambda = 1.08$; experiment conducted based on Fig. 7

function, (7), is chosen, instead of common ansatz $\psi_{\text{vol}}(J) = K/2(J-1)^2$. Further, following (Nolan et al., 2014)

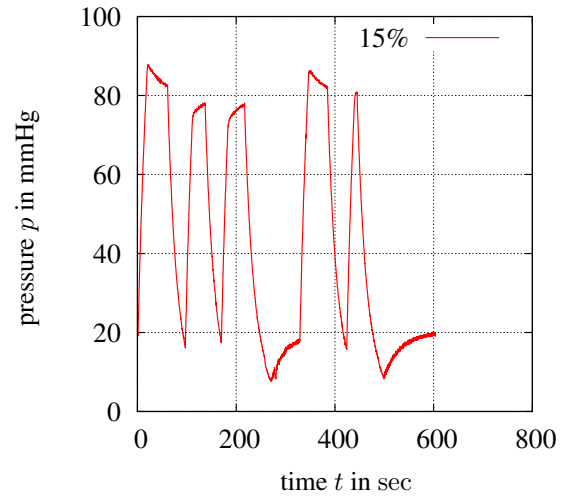
$$\psi_{\text{aniso}}(\mathbf{C}, \mathbf{M}_0, \mathbf{M}_1) = \frac{k_1}{2k_2} \left(\left(e^{k_2(I_4-1)^2} - 1 \right) + \left(e^{k_2(I_6-1)^2} - 1 \right) \right) \quad (9)$$

is chosen. In conclusion, we have the material parameters K , c_{10} , k_1 and k_2 . Using the strain-energy function, the second Piola-Kirchhoff stress tensor reads

$$\tilde{\mathbf{T}} = 2 \frac{\partial \psi(J, \bar{\mathbf{C}}, \mathbf{M}_0, \mathbf{M}_1)}{\partial \mathbf{C}} = 2 \left(\frac{d\psi_{\text{isoch}}(\bar{\mathbf{C}})}{d\mathbf{C}} + \frac{d\psi_{\text{vol}}(J)}{d\mathbf{C}} + \frac{\partial \psi_{\text{aniso}}(\mathbf{C}, \mathbf{M}_0, \mathbf{M}_1)}{\partial \mathbf{C}} \right). \quad (10)$$



(a) Stage 11: Axial force vs pressure



(b) Stage 11: Pressure vs time

Figure 18: Stage 11: pressure varies from 10 to 80mmHg ; $\lambda = 1.15$; experiment conducted based on Fig. 7

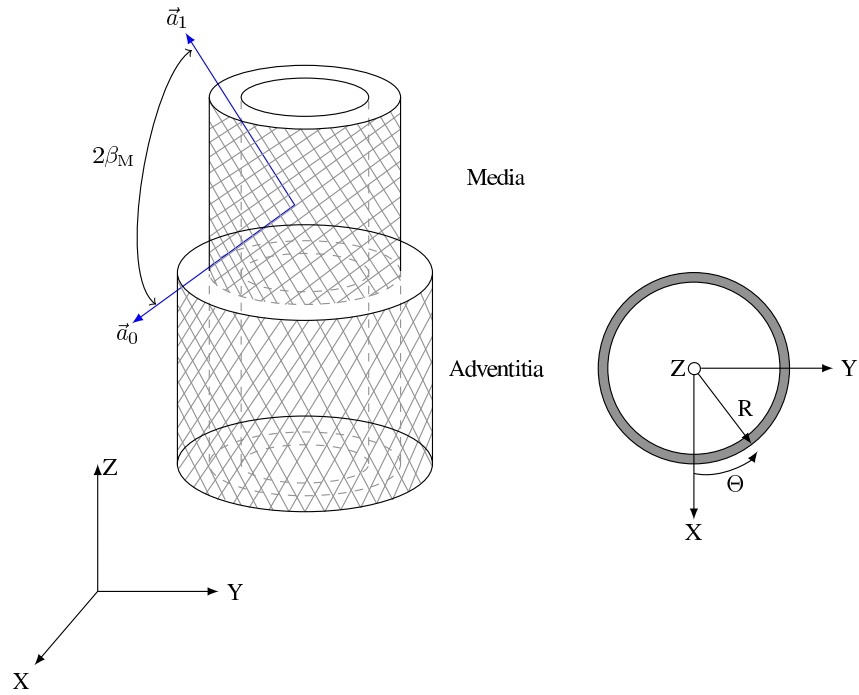


Figure 19: Helical fibers in an artery

Next, we derive the derivatives. From Eq.(8) we derive

$$\begin{aligned}
 D_{\mathbf{C}}\psi_{\text{isoch}}(\mathbf{C})[\mathbf{H}] &= D_{\mathbf{C}}c_{10}(\text{tr } \mathbf{C})(\det \mathbf{C})^{-1/3}[\mathbf{H}] \\
 &= c_{10} \left(-\frac{1}{3}(\text{tr } \mathbf{C})(\det \mathbf{C})^{-4/3} D_{\mathbf{C}}(\det \mathbf{C})[\mathbf{H}] + (\det \mathbf{C})^{-1/3} D_{\mathbf{C}} \text{tr } \mathbf{C}[\mathbf{H}] \right) \\
 &= c_{10} \left(-\frac{1}{3}(\text{tr } \mathbf{C})(\det \mathbf{C})^{-4/3}(\det \mathbf{C})(\mathbf{C}^{-1} \cdot \mathbf{H}) + (\det \mathbf{C})^{-1/3} \mathbf{I} \cdot \mathbf{H} \right) \\
 \Rightarrow \frac{d\psi_{\text{isoch}}}{d\mathbf{C}} &= c_{10} \left(-\frac{1}{3}(\text{tr } \mathbf{C})(\det \mathbf{C})^{-1/3} \mathbf{C}^{-1} + (\det \mathbf{C})^{-1/3} \mathbf{I} \right)
 \end{aligned} \tag{11}$$

and from Eq.(7), we obtain

$$\begin{aligned} D_{\mathbf{C}}\psi_{\text{vol}}(\mathbf{C})[\mathbf{H}] &= \frac{K}{50} D_{\mathbf{C}}\left((\det \mathbf{C})^{5/2} + (\det \mathbf{C})^{-5/2} - 2\right)[\mathbf{H}] \\ &= \frac{K}{50} \left(-\frac{5}{2}(\det \mathbf{C})^{-6/2}\mathbf{C}^{-1} + \frac{5}{2}(\det \mathbf{C})^{4/2}\mathbf{C}^{-1}\right) \cdot \mathbf{H} \\ \Rightarrow \frac{d\psi_{\text{vol}}}{d\mathbf{C}} &= \frac{K}{20} (J^4 - J^{-6})\mathbf{C}^{-1}. \end{aligned} \quad (12)$$

Using Eq.(9) we calculate the third term in Eq.(10)

$$\frac{\partial\psi_{\text{aniso}}}{\partial\mathbf{C}} = k_1 \left((I_4 - 1)e^{k_2(I_4-1)^2} \mathbf{M}_0 + (I_6 - 1)e^{k_2(I_6-1)^2} \mathbf{M}_1 \right). \quad (13)$$

The expressions (11)-(13) are substituted in Eq.(10), leading to

$$\begin{aligned} \tilde{\mathbf{T}} &= \frac{K}{10} (J^5 - J^{-5})\mathbf{C}^{-1} + J^{-2/3}c_{10} \left(-\frac{1}{3}(\text{tr } \mathbf{C})\mathbf{C}^{-1} + \mathbf{I} \right) \\ &\quad + 2k_1 \left((I_4 - 1)e^{k_2(I_4-1)^2} \mathbf{M}_0 + (I_6 - 1)e^{k_2(I_6-1)^2} \mathbf{M}_1 \right). \end{aligned} \quad (14)$$

is obtained. Using the push-forward operation of the 2nd PK, the Cauchy stress tensor reads

$$\begin{aligned} \mathbf{T} &= \frac{1}{J} \tilde{\mathbf{T}} \mathbf{F} \mathbf{F}^T = \frac{K}{10} (J^4 - J^{-6})\mathbf{I} + c_{10} J^{-2/3} \overline{\mathbf{B}}^D \\ &\quad + 2J^{-1}k_1 \left((I_4 - 1)e^{k_2(I_4-1)^2} \mathbf{M}_0 + (I_6 - 1)e^{k_2(I_6-1)^2} \mathbf{M}_1 \right), \end{aligned} \quad (15)$$

containing an isotropic part (the first two terms) and an anisotropic part (part featuring the structural tensors \mathbf{M}_0 and \mathbf{M}_1). This material model has to be adapted to the media and the adventitia in such a way that $2 \times 4 = 8$ (K , c_{10} , k_1 , k_2 for each layer) material parameters have to be determined. K can be interpreted as the bulk and c_{01} as shear moduli of the material's isotropic part. k_1 and k_2 control the "stiffness" in both fiber directions. If the angles β are also assumed to be unknown, this increases the number of material parameters to be identified by two additional parameters.

5 Material Parameter Identification

On the basis of the experimental data, the material parameters, K^A , c_{10}^A , k_1^A , k_2^A and K^M , c_{10}^M , k_1^M , k_2^M have to be identified ('A' stands for the adventitia, while 'M' refers to the media). Here, we assume that the angles β are given. The experiment provides the axial reaction force as well as the radial displacement of the artery's contour (in the plane) under inflation for different loading cycles. Since we are – at least in a first step – only interested in the elastic response, a mean value of the curve is chosen. The axial displacements and the internal pressure are prescribed, see Fig. 20. This experimental data is used to adjust the structural response of the finite element model, i.e. to determine the material parameters of each layer. In other words, the material parameters are optimized in such a way that the residual between the experimental and the simulated data is minimized in the sense of a least-square method. The application of optimization tools – for the purpose of material parameter identification using the response of entire finite element simulation – can, for example, be found in (Mahnken and Stein, 1996; Kreißig, 1998; Scheday, 2003) and (Hartmann et al., 2003), as well as the references cited therein.

5.1 Methodology

$\boldsymbol{\kappa} \in \mathbb{R}^{n_{\boldsymbol{\kappa}}}$ contains $n_{\boldsymbol{\kappa}}$ material parameters, that we are interested in. The vector

$$\mathbf{d} = \left\{ \begin{array}{c} \mathbf{d}^1 \\ \mathbf{d}^2 \\ \vdots \\ \mathbf{d}^{n_{\text{exp}}} \end{array} \right\}, \quad \mathbf{d} \in \mathbb{R}^{n_D} \quad (16)$$

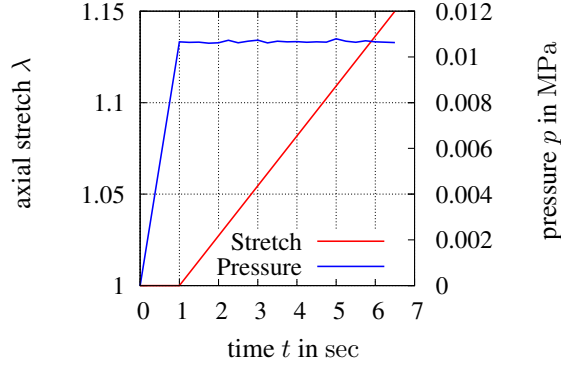


Figure 20: The prescribed axial stretch and internal pressure

comprises all experimental data, and it is sub-divided in several experimental observations $\mathbf{d}^e \in \mathbb{R}^{n_d^e}$, $e = 1, \dots, n_{\text{exp}}$. In each of the experiments, we have a set of measurements for each point in time, i.e. at the discrete times we measure – in our case – the axial force F_k^e and the radial displacements $\mathbf{u}_k^e \in \mathbb{R}^{n_{uk}^e}$. These are assembled into the vectors

$$\mathbf{d}^e = \begin{Bmatrix} \mathbf{d}_1^e \\ \vdots \\ \mathbf{d}_{n_t^e}^e \end{Bmatrix} \in \mathbb{R}^{n_d^e}, \quad \mathbf{d}_k^e = \begin{Bmatrix} F_k^e \\ \mathbf{u}_k^e \end{Bmatrix} \in \mathbb{R}^{1+n_{uk}^e} \quad (17)$$

with $k = 1, \dots, n_t^e$ (n_t^e is the number of evaluation points in time of experiment e). In total, we have $n_D = \sum_{e=1}^{n_{\text{exp}}} \sum_{k=1}^{n_t^e} (1 + n_{uk}^e)$ data points.

Equivalently, we have data $\hat{\mathbf{s}}^e(\boldsymbol{\kappa})$ of the finite element simulation for each “experiment” e . The data is projected both spatially and temporally (in this case by linear interpolation) onto the experimental time data, $\mathbf{s}^e(\boldsymbol{\kappa}) = \mathcal{P}[\hat{\mathbf{s}}^e(\boldsymbol{\kappa})] \in \mathbb{R}^{n_d^e}$, where the entire model data

$$\mathbf{s}(\boldsymbol{\kappa}) = \begin{Bmatrix} \mathbf{s}^1(\boldsymbol{\kappa}) \\ \mathbf{s}^2(\boldsymbol{\kappa}) \\ \vdots \\ \mathbf{s}^{n_{\text{exp}}}(\boldsymbol{\kappa}) \end{Bmatrix}, \quad \mathbf{s} \in \mathbb{R}^{n_D} \quad (18)$$

depends on $\boldsymbol{\kappa}$.

Since the material data vectors have different magnitudes, physical units, and different sizes n_d^e , we introduce the weighting of the residual between the model and experimental data $\hat{\mathbf{r}}(\boldsymbol{\kappa}) = \mathbf{s}(\boldsymbol{\kappa}) - \mathbf{d}$ by the weighting matrix $\mathbf{W} \in \mathbb{R}^{n_D \times n_D}$,

$$\mathbf{r}(\boldsymbol{\kappa}) = \mathbf{W}\hat{\mathbf{r}}(\boldsymbol{\kappa}) = \mathbf{W}\{\mathbf{s}(\boldsymbol{\kappa}) - \mathbf{d}\}. \quad (19)$$

The weighting matrix is constructed by the following sub-matrices,

$$\mathbf{W} = \begin{bmatrix} \mathbf{W}^1 & & \\ & \ddots & \\ & & \mathbf{W}^{n_{\text{exp}}} \end{bmatrix}, \quad \mathbf{W}^e = \begin{bmatrix} \mathbf{W}_1^e & & \\ & \ddots & \\ & & \mathbf{W}_{n_t^e}^e \end{bmatrix} \quad (20)$$

with

$$\mathbf{W}_k^e = \begin{bmatrix} \alpha_k^e & \\ & \beta_k^e \mathbf{I} \end{bmatrix}, \quad \alpha_k^e = \frac{1}{\max_k |F_k^e| n_t^e}, \quad \beta_k^e = \frac{1}{\max_k (\max_j |u_{kj}^e|) n_{uk}^e n_t^e}$$

The weighted residual vector $\mathbf{r}(\boldsymbol{\kappa})$ has to be minimized in the least-square sense. In other words, the objective function $f(\boldsymbol{\kappa}) = (1/2)\mathbf{r}^T\mathbf{r}$ is minimized, see (Daniels, 1978; Dennis and Schnabel, 1996; Nocedal and Wright, 2006; Butenko and Pardalos, 2014),

$$\begin{aligned}\min_{\boldsymbol{\kappa}} f(\boldsymbol{\kappa}) &= \min_{\boldsymbol{\kappa}} \frac{1}{2} \|\mathbf{r}(\boldsymbol{\kappa})\|_2^2 \\ &= \min_{\boldsymbol{\kappa}} \frac{1}{2} \mathbf{r}^T \mathbf{r} \\ &= \min_{\boldsymbol{\kappa}} \frac{1}{2} (\mathbf{W}\{\mathbf{s}(\boldsymbol{\kappa}) - \mathbf{d}\})^T \mathbf{W}\{\mathbf{s}(\boldsymbol{\kappa}) - \mathbf{d}\}.\end{aligned}\quad (22)$$

According to (Dennis and Schnabel, 1996), the necessary condition to obtain a minimum,

$$\text{grad}_{\boldsymbol{\kappa}} f(\boldsymbol{\kappa}) = \mathbf{J}^T(\boldsymbol{\kappa}^*)\mathbf{r}(\boldsymbol{\kappa}^*) \stackrel{!}{=} \mathbf{0}, \quad (23)$$

has to be satisfied. $\mathbf{J}(\boldsymbol{\kappa}) = d\mathbf{r}(\boldsymbol{\kappa})/d\boldsymbol{\kappa}$ defines the Jacobian. Additionally, the material parameters are constrained by upper and lower bound values. Thus, the final problem is

$$\min_{\boldsymbol{\kappa}} \frac{1}{2} \|\mathbf{r}(\boldsymbol{\kappa})\|_2^2 \quad \text{where } \kappa_{\min_i} \leq \kappa_i \leq \kappa_{\max_i}, i = 1, \dots, n_{\boldsymbol{\kappa}}. \quad (24)$$

κ_{\min_i} and κ_{\max_i} are the minimum and the maximum value of each parameter. Eq.(22) is a non-linear least squares problem, continuously leading to multiple solutions. There are a number of numerical methods to solve such problems. In this particular case, the trust-region-reflective algorithm implemented in Matlab (lsqnonlin.m) is used to find the best fit. A Matlab script calls the finite element program, in which the constitutive model is implemented. The material parameters are adjusted after each iteration until the optimality condition is reached.

5.2 Measures of Optimization Quality

Eq.(22) is an ill-posed problem and consequently, unique solutions cannot be expected. Naturally, the question regarding the quality of the results arises. Certain indicators can help to get a better understanding of the final results. They are the confidence interval, correlation between the identified material parameters, and the coefficient of determination, see (Krämer et al., 2015) in the context of material parameter identification.

Confidence Interval The purpose of using a confidence interval is to identify the possible range of values for the parameter of interest. In order to calculate the interval, the non-linear model is approximated – leading to a linear approximation at the optimized parameter $\boldsymbol{\kappa}^*$, see (Krämer et al., 2015),

$$\mathbf{r}(\boldsymbol{\kappa}) = \mathbf{r}(\boldsymbol{\kappa}^*) + \mathbf{J}(\boldsymbol{\kappa}^*)(\boldsymbol{\kappa} - \boldsymbol{\kappa}^*). \quad (25)$$

The symmetric covariance matrix is approximated by

$$\mathbf{P} \approx \sigma^2 [\mathbf{J}^T(\boldsymbol{\kappa}^*)\mathbf{J}(\boldsymbol{\kappa}^*)]^{-1} \quad (26)$$

where σ is the standard deviation and σ^2 denotes the variance defined by

$$\sigma^2 = \frac{1}{n_D - 1} \sum_{i=1}^{n_D} (r_i - \bar{r})^2, \quad (27)$$

with the mean-value $\bar{r} = (\sum_{i=1}^{n_D} r_i)/n_D$. Covariance is a measure of how a change in one parameter affects the other material parameter. Specifically, it measures the degree to which two parameters are linearly associated. It gives an idea about how the model responds to changes in two parameters. A positive covariance implies that the two parameters vary directly, whereas negative covariance signifies that the two parameters vary inversely. The covariance matrix reads

$$\mathbf{P} = \begin{bmatrix} \sigma_{\kappa_1}^2 & \text{COV}(\kappa_1, \kappa_2) & \dots & \text{COV}(\kappa_1, \kappa_m) \\ & \sigma_{\kappa_2}^2 & \dots & \text{COV}(\kappa_2, \kappa_m) \\ & & \ddots & \vdots \\ \text{sym} & & & \sigma_{\kappa_m}^2 \end{bmatrix}.$$

The range of the confidence interval is determined by taking the square root of the leading diagonal elements of the covariance matrix. Therefore, the confidence interval of the parameter κ_i is

$$\kappa_i^{\text{conf}} = \kappa_i^* \pm \Delta\kappa_i^* \in \mathbb{R}^{n_{\boldsymbol{\kappa}}} \quad \text{with } \Delta\kappa_i^* = \sqrt{\sigma_{\kappa_i}^2} \in \mathbb{R}^{n_{\boldsymbol{\kappa}}}, i = 1, \dots, m. \quad (28)$$

Correlation Coefficient The covariance matrix \mathbf{P} contains information about the correlation between two material parameters κ_i and κ_j . To get a better idea about the correlation between parameters, the correlation matrix \mathbf{K} is calculated from the covariance matrix by

$$K_{ij} = \frac{P_{ij}}{\sqrt{P_{ii}P_{jj}}} =: \text{corr}(\kappa_i, \kappa_j) \quad (29)$$

It is clear that $k_{ii} = 1$ and the non-diagonal elements k_{ij} determine the degree to which the two material parameters are linearly correlated and lie in the interval $[-1, 1]$. The correlation matrix reads

$$\mathbf{K} = \begin{bmatrix} 1 & \text{corr}(\kappa_1, \kappa_2) & \dots & \text{corr}(\kappa_1, \kappa_m) \\ & 1 & & \text{corr}(\kappa_2, \kappa_m) \\ & & \ddots & \\ \text{sym} & & & 1 \end{bmatrix}.$$

If $K_{ij} = 1$, $i \neq j$, this indicates that the parameter κ_i and κ_j depend on each other. A positive correlation indicates that one parameter depends directly on the other. Furthermore, a negative correlation indicates inverse proportionality among the two parameters. A strong correlation can be seen for $k_{ij} \geq 0.8$.

Coefficient of Determination Coefficient of determination is the measure of how well a model fits the data. The coefficient is also known as R -squared, or R^2 , and is used as a guideline to measure the accuracy of the model. R^2 is defined by

$$R^2 = 1 - \frac{\sum_{i=1}^{n_D} (d_i - s_i)^2}{\sum_{i=1}^{n_D} (d_i - \bar{d})^2} \quad \text{with} \quad \bar{d} = \frac{1}{n_D} \sum_{i=1}^{n_D} d_i, \quad (30)$$

see, for example, (Draper and Smith, 1998). The coefficient R^2 is expressed as a value between zero and one. The value of one indicates a perfect fit. On the other hand, if the value is close to zero, this indicates that the model fails to predict accurately. Even though it is advised to keep the value of R^2 in the vicinity of one, this does not mean that this value alone will determine the quality of the fit, see (Anscombe, 1973).

However, the indicators κ^{conf} of Eq.(28), K_{ij} of Eq.(29) and R^2 of Eq.(30) are chosen as quality measures of the material parameter identification process.

5.3 Application to the Experiment

The experiments are conducted based on the loading protocol discussed in Section 3, see Fig. 21. The output from the experiment are the axial reaction force and the radial displacements taken from the High Resolution (HR) photos using a contour detection program, see Fig. 1(a) and Fig. 1(b). The contour detection program uses the OpenCV implementation of Suzuki and Abe (1985). The program develops an ASCII file based on the photo. A contour can be seen in the Fig. 22(b). Using the data from the contour detection program, a 3D-model is created using the pre- and post-processing software GiD (GiD-Manual, 2012), see Fig. 22(c). One of the basic problems is to be seen in the bubbles in the fluid. These bubbles are manually cut out in order to obtain reasonable results. For creation of the finite element model a total of 100 points (50 points on the left and 50 points on the right side) are chosen using the first picture of the process. The wall thickness is chosen to be constant over the height and in circumferential direction. As the thickness of the media and the adventitia are unknown, a ratio of 3:1 is assumed based on (Rhodin, 2011).

The mean loading cycle of stage 8 serves as a basis for the identification process, see Fig. 15. Only one loading cycle of the stage is used (which lasts for 6.05 sec) since hyperelastic materials are time-independent, see Fig. 23. In this context, the time is only a parameter to control the load step-size. The information is available for 22 steps between 0 – 6.5 sec. Together, the mean axial reaction force, F_k^e , at each time step as well as the mean radial displacement, $d_{\kappa_m}^e$, taken from the contour (available from 30 images), serve to form the experimental data vector $\mathbf{d} \in \mathbb{R}^{n_d}$.

Since we have to compare the finite element result of the radial displacement with the discrete data of the experiment, there must be a projection. We project the nodal coordinates of the finite element mesh onto the experimental contour line. This is explained in Appendix A. For our example, we chose 20-noded hexahedral elements (4000 elements, 18100 nodes).

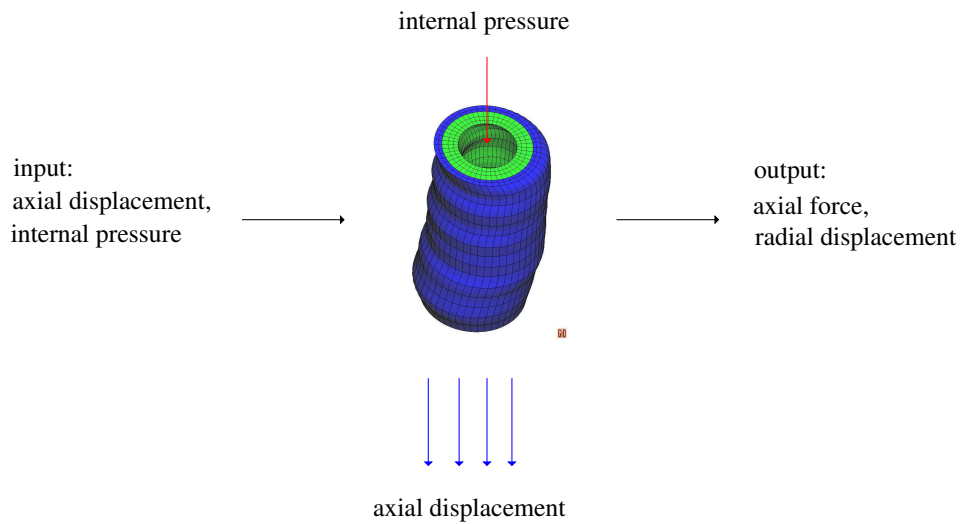
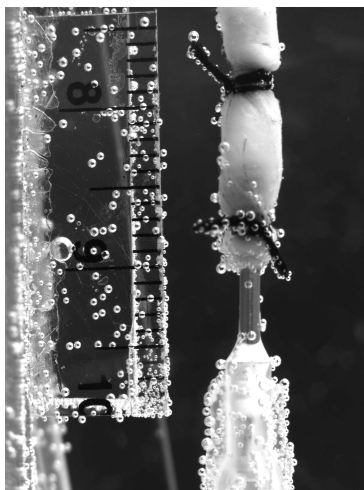


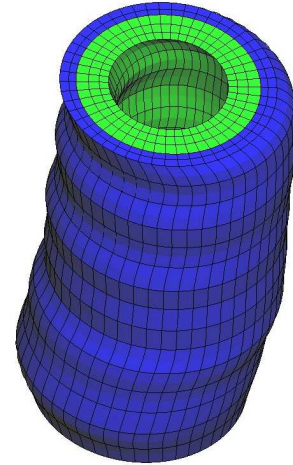
Figure 21: Input and output of the simulation



(a) Photo of the artery using HR camera



(b) Contour detection of Fig. 22(a)



(c) 3D model of the artery using contour lines of Fig. 22(b). Number of nodes= 18100

Figure 22: Image processing and geometry determination

As a first step, an initial guess of the parameters is necessary to start the iterative process. The initial guess provided to the optimizer is compiled in Tab. 2.

Initial guess	
Adventitia	Media
$K^A = 1 \text{ MPa}$	$K^M = 4 \text{ MPa}$
$c_{10}^A = 0.08171 \text{ MPa}$	$c_{10}^M = 0.245 \text{ MPa}$
$k_1^A = 0.0051 \text{ MPa}$	$k_1^M = 0.000034 \text{ MPa}$
$k_2^A = 0.154$	$k_2^M = 0.354$

Table 2: Initial guess of the material parameters to be identified

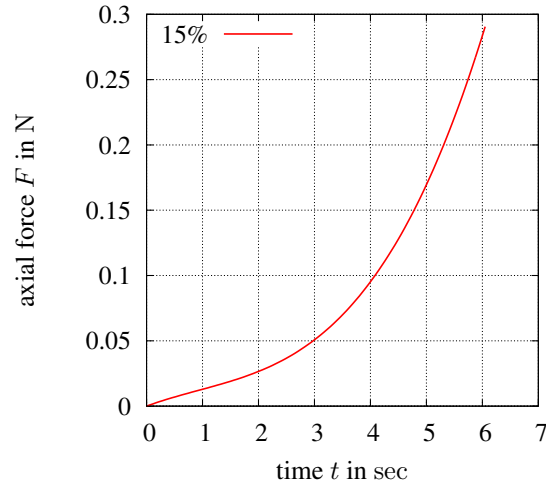


Figure 23: Mean loading path of stage 8 - used for optimization

The trust-region algorithm implemented in Matlab is used for the sake of optimization. A Matlab program calls the *lsqnonlin.m* routine (pre-programmed in Matlab) which, after each iteration, changes the value of the material parameter according to its algorithmic structure- and the finite element program is started using the newly updated parameters. This process continues until the optimality condition is achieved. The angle of helix in the media is assumed to be $\beta_m = 20^\circ$ and the angle of helix in the adventitia is assumed to be $\beta_a = 60^\circ$, see Fig. 1(b).

In order to determine the radial displacement, 14 nodes are taken from each side of the artery, see Fig. 22(b). In order to determine the axial reaction force, all nodal reaction forces on the top side of the discretized artery (nodal coordinates) are summed up. The sum represents the total reaction force at the surface, which is compared to the reaction force measured from the load cell of the experiment.

6 Results

The material parameters of the simulation are calibrated to the experimental data, see Fig. 23. The optimization is achieved when the relative change in the objective function is less than 10^{-6} . The entire optimization procedure takes almost 6 hours to complete using a 1200 MHz PC with 32 processors. The material parameters, after optimization, are compiled in Tab. 3. The confidence intervals of some material parameters are totally unsatisfactory

After optimization	
Adventitia	Media
$K^A = 0.120001 \pm 6729678 \text{ MPa}$	$K^M = 3.358939 \pm 1103.743 \text{ MPa}$
$c_{10}^A = 0.08171 \pm 0.00014184 \text{ MPa}$	$c_{10}^M = 0.1294158 \pm 0.075637 \text{ MPa}$
$k_1^A = 0.05618226 \pm 0.05085427 \text{ MPa}$	$k_1^M = 0.000485767 \pm 0.000022859 \text{ MPa}$
$k_2^A = 0.1507043 \pm 4393.991$	$k_2^M = 0.3542526 \pm 289491.2$

Table 3: Material parameters after optimization

(K^A , k_2^A , K^M and k_2^M).

Tab. 4 lists the correlation values for the material parameters of the different layers. It can be seen that there are strong correlations between the material parameters except for the bulk modulus of the adventitia. The parameter K^A shows a very low correlation with the other parameters. However, all the other parameters are more significantly correlated to each other, whether it is a positive or a negative correlation - although the coefficient of determination, $R^2 = 0.99$ indicates a very good fit, see Fig. 24. Moreover, the confidence intervals for the bulk

Correlation table								
	K^A	c_{10}^A	k_1^A	k_2^A	K^M	c_{10}^M	k_1^M	k_2^M
K^A	1.0000	0.1987	0.1874	-0.1809	-0.1277	0.1313	-0.2051	0.1951
c_{10}^A		1.0000	0.9901	-0.9911	-0.8816	0.9014	-0.9900	0.9601
k_1^A			1.0000	-0.9939	-0.8626	0.8839	-0.9933	0.9405
k_2^A				1.0000	0.8676	-0.8914	0.9797	-0.9274
K^M					1.0000	-0.9978	0.8628	-0.8353
c_{10}^M						1.0000	-0.8813	0.8478
k_1^M							1.0000	-0.9627
k_2^M								1.0000

Weak correlation Strong correlation

Table 4: Correlation between material parameters

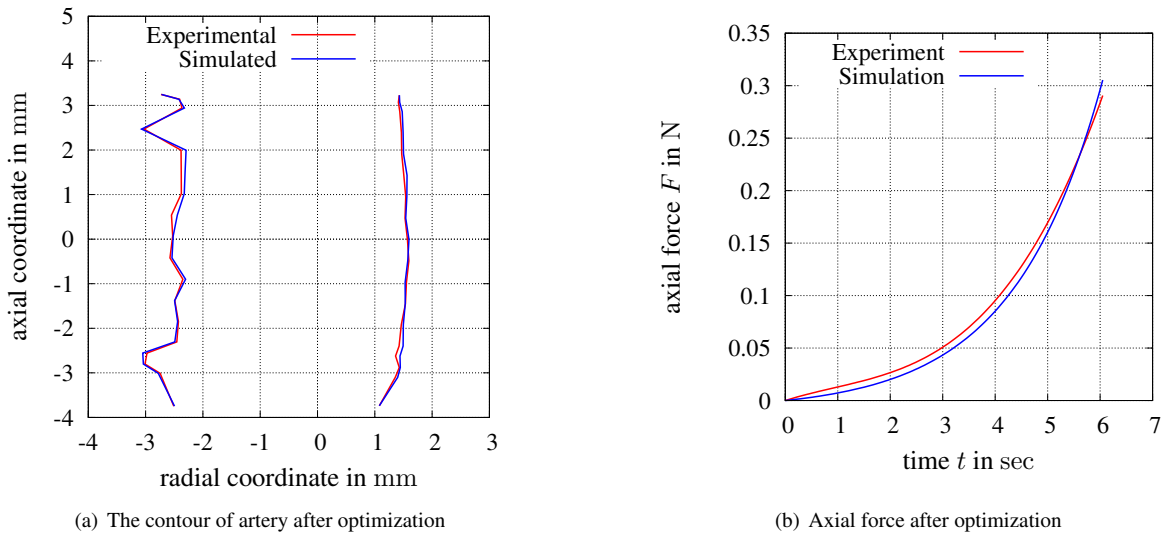


Figure 24: Result of optimization

moduli K and the k_2 for both media and adventitia are extremely unsatisfactory. Fig. 24(a) shows a comparison of contours after optimization. Apparently, the optimization is satisfactory (corresponding to the R^2 value). Fig. 24(b) shows the axial force after optimization, indicating a good result as well.

Based on the results, it can be noticed that parameters of the models are related to each other. The genuine lack of information inhibits a proper identification of parameters. The basic question is how we could obtain reliable parameters of each layers. Thus, the first step is to find out whether the problem is inherent in the lack of data. It must be concluded that the experiments should be performed on each of the layers, which, unfortunately, is an extremely challenging task in the case of mammary arteries and radial arteries (the most commonly used arteries for bypass surgeries). A strong correlation amongst the parameters also indicates that the constitutive model is either over-parametrized (here, we chose the most simple model of anisotropy) or that a different type of experiment is required to properly identify the material parameters. In this case, since each material parameter has a physical significance it may be concluded that a different type of experiment is required to study the material parameters.

Pure isotropy in each layer In a first computation, we reduce the material parameters and assume only isotropy in each layer - implying that the material parameters K^A , c_{10}^A and K^M , c_{10}^M are identified. The material parameters, after optimization, are compiled in Tab. 5. The coefficient of determination in this case is 0.822 which represents a good fit. According to Tab. 6 there is no strong correlation between the material parameters except K^M and c_{10}^M .

Adventitia	Media
$K^A = 0.004764536 \pm 5248110$ MPa	$K^M = 2.907458 \pm 377.6767$ MPa
$c_{10}^A = 0.0008528 \pm 0.00001268626$ MPa	$c_{10}^M = 0.1313374 \pm 0.03293763$ MPa

Table 5: Material parameters for purely isotropic material, after optimization

Correlation table				
	K^A	c_{10}^A	K^M	c_{10}^M
K^A	1.0000	-0.3873	-0.0251	0.0319
c_{10}^A		1.0000	-0.6864	0.6603
K^M			1.0000	-0.9972
c_{10}^M				1.0000

Table 6: Correlation between material parameters for purely isotropic material

Weak correlation Strong correlation

However, the confidence intervals for the bulk moduli are not satisfactory. Fig. 25 shows the contour and the axial

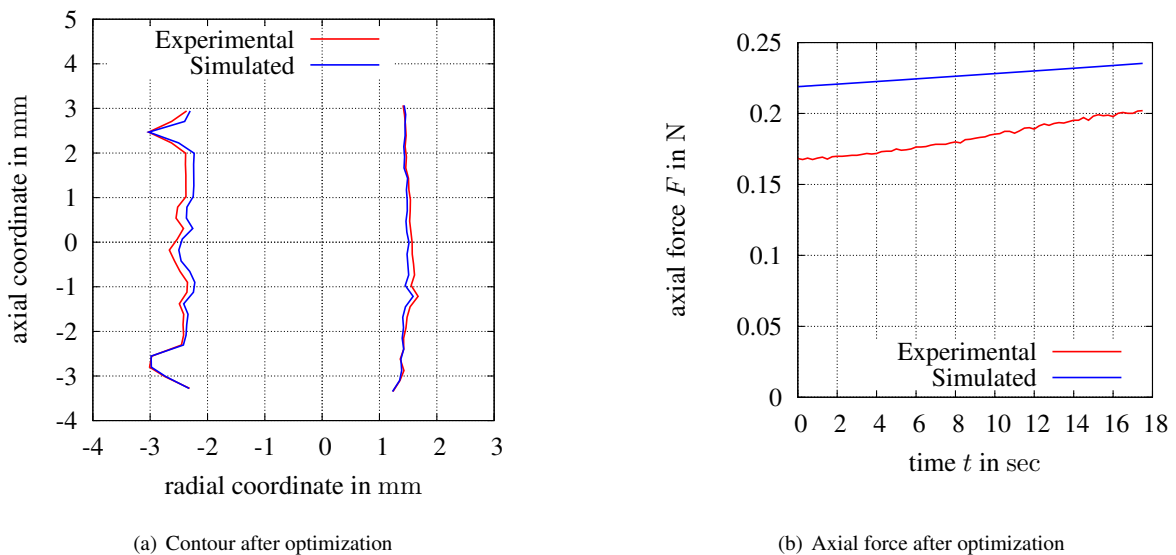


Figure 25: Arterial wall with two layers, isotropic across each layer

force after optimization.

Purely homogeneous isotropic material As the previous results suggest to investigate an artery consisting of only one material, only the two material parameters K and c_{10} need to be identified. The initial values are assumed to be $K_{initial} = 1.2$ MPa and $c_{10_{initial}} = 0.0817$ MPa. The coefficient of determination obtained after the optimization is 0.791 - indicating a decent fit. However, the confidence interval for the bulk modulus is very high as can be seen from Tab. 7. The result shows that there is only a very low correlation of 0.6228 between the material parameters K and c_{10} . The contour and the axial force after optimization can be seen in Fig. 26. Thus, the outcome of the identification process is unsatisfactory as well – since the experiments don't appear to address the bulk modulus very well.

In conclusion, the inflation and the axial extension of the artery in connection with the measurements of the radial displacements and the axial force do not lead to reliable material parameters with regard to the material properties of each individual layer.

After optimization
$K = 0.5275 \pm 1.5926 \times 10^9 \text{ MPa}$
$c_{10} = 0.04448 \pm 0.0004262 \text{ MPa}$

Table 7: Material parameters for purely homogeneous isotropic material, after optimization

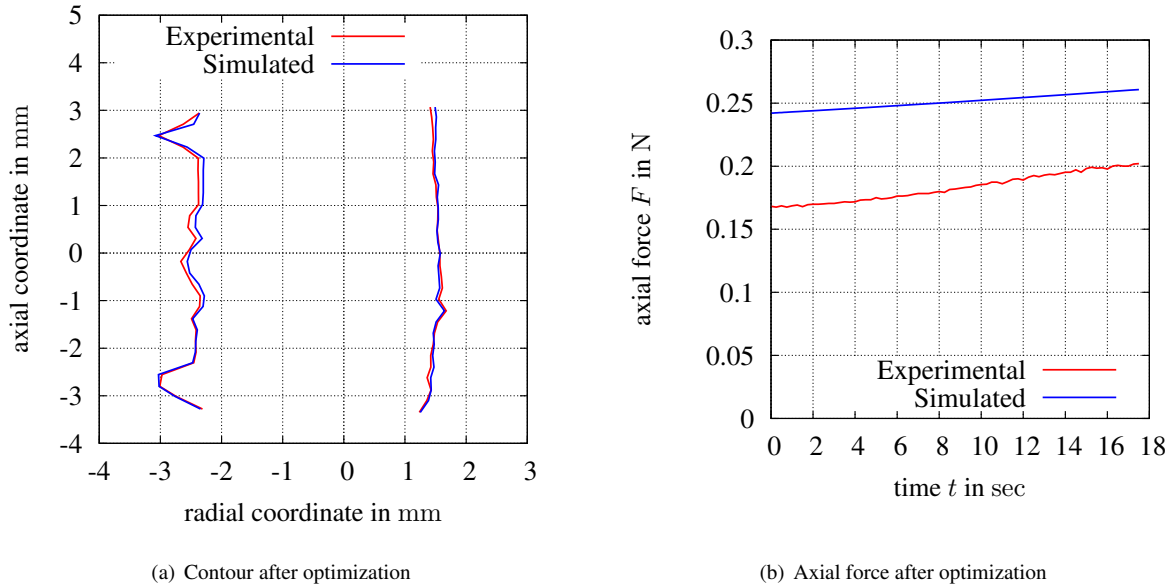


Figure 26: Arterial wall with one layer, homogeneous across the wall

7 Conclusions

In a first step, a human mammary artery is exposed to cyclic loading paths in a new testing device – with varying axial displacements and internal pressure rates – in order to determine the rate-dependent material properties. It turns out that viscoelastic material properties are essential. Since the main goal of this paper is to identify the material parameters of a two-layered, anisotropic artery with an arbitrary geometry, we restrict ourselves to hyperelasticity. The simplest constitutive model for a material with two fiber directions contains four material parameter of each layer (media and adventitia). The thickness of the layers and the thickness over the specimen's height are not known and, accordingly, are uncertain. Moreover, the directions of anisotropy are not known a priori. Therefore, the unknown quantities are estimated based on literature references. Using digital images and a force device in the experiment for given axial displacements and internal pressure, the resulting deformation of the contour and the axial forces are compared with finite element computations. Quality measures using an optimization tool reveal that some of the material parameters are correlated, while others exhibit totally unsatisfactory confidence intervals. In other words, it was not yet possible to attribute exact material properties to the media and the adventitia – although we assumed certain experimental data. Thus, it must be concluded that further tests will be necessary to reliably identify the different layers, fiber orientations, materials, as well as the geometrical properties. This is one of the key problems in soft-tissue modeling.

We gratefully acknowledge the financial support provided by the German-Israeli Foundation (GIF, grant no. I-89-202.17-2012)

A Projection from simulation to experiment

In this section, the calculations behind the projection of simulated data to experimental data is explained. Both the simulation and the experimental data are analyzed at time t . There should be a reference point \bar{C}_{ref} which is same

in both data. In this particular case, the reference point is taken as the mid point of the bottom of the artery at which location it is clamped to the needle. This point of the artery has no displacement and remains the same throughout the experiment and the simulation. The objective is to project a node $\vec{r}_i \in \mathcal{S}$ lying on the finite element line \mathcal{S} onto the experimental data line \mathcal{E} . The projected point is $\hat{r}'(\Theta) \in \mathcal{E}$, see Fig. 27. This implies that the projection

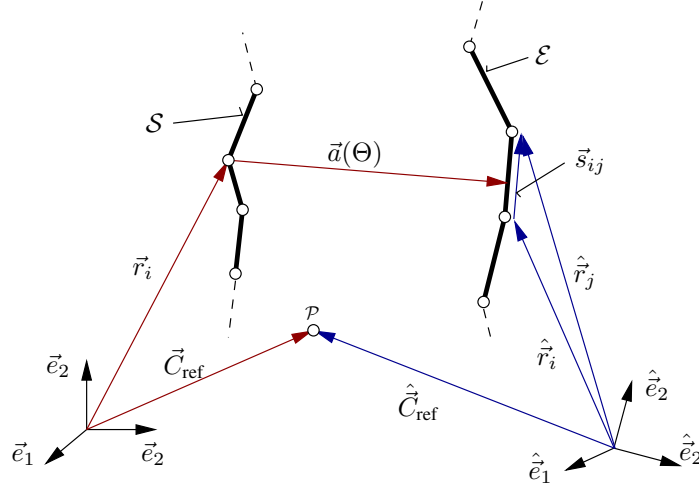


Figure 27: Projection of finite element node (line \mathcal{S}) onto experimental contour line \mathcal{E}

vector $\vec{a}(\Theta)$ is perpendicular to the experimental data line and the norm is minimized, see (Hartmann and Sguazzo, 2015). In order to project the data from the simulation to the experimental line, the norm of the projection vector has to be minimized,

$$\|\vec{a}(\Theta)\| \rightarrow \min \quad (31)$$

where,

$$\vec{a}(\Theta) = \hat{r}'(\Theta) - \hat{C}_{\text{ref}} - (\vec{r}_i - \vec{C}_{\text{ref}}) \quad (32)$$

with

$$\hat{r}'(\Theta) = \hat{r}_i + \Theta(\hat{r}_j - \hat{r}_i) = \hat{r}_i + \Theta(\vec{s}_{ij}) \quad \text{with} \quad \vec{s}_{ij} = \hat{r}_j - \hat{r}_i. \quad (33)$$

This is a typical least-square problem where the objective function

$$f(\Theta) = \frac{1}{2} \vec{a}(\Theta) \cdot \vec{a}(\Theta) \quad (34)$$

is to be minimized. The necessary condition implies that the vanishing Gateaux-differential,

$$Df(\Theta)[h] = \vec{a}'(\Theta) \cdot \vec{a}(\Theta) h = 0. \quad (35)$$

In view of Eq.(32) this is equivalent to

$$\hat{r}'(\Theta^*) \cdot \vec{a}(\Theta^*) = 0, \quad (36)$$

where Θ^* is the line parameter of the projection on the experimental line. We assume the orthogonality

$$\hat{r}'(\Theta) = \vec{s}_{ij} \implies \vec{s}_{ij} \cdot \vec{a}(\Theta^*) = 0. \quad (37)$$

The projection vector Eq.(32) reads

$$\vec{a}(\Theta^*) = \hat{r}_i + \Theta^* \vec{s}_{ij} - \hat{C}_{\text{ref}} - (\vec{r}_i - \vec{C}_{\text{ref}}). \quad (38)$$

Multiplying Eq.(38) with \vec{s}_{ij} leads to

$$\vec{a}(\Theta^*) \cdot \vec{s}_{ij} = \hat{r}_i \cdot \vec{s}_{ij} + \Theta^* \vec{s}_{ij} \cdot \vec{s}_{ij} - \hat{C}_{\text{ref}} \cdot \vec{s}_{ij} - (\vec{r}_i - \vec{C}_{\text{ref}}) \cdot \vec{s}_{ij}. \quad (39)$$

Substituting Eq.(37) into Eq.(39)

$$\Theta^* |\vec{s}_{ij}|^2 - (\vec{r}_i - \vec{C}_{\text{ref}} - (\hat{r}_i - \hat{C}_{\text{ref}})) \cdot \vec{s}_{ij} = 0. \quad (40)$$

Finally, the line parameter of the desired projection point

$$\Theta^* = \frac{(\vec{r}_i - \vec{C}_{\text{ref}} - (\hat{r}_i - \hat{C}_{\text{ref}})) \cdot \vec{s}_{ij}}{|\vec{s}_{ij}|^2} \quad (41)$$

is obtained. The displacement of this point is interpolated from the neighboring two points on the experimental line,

$$\hat{u}(\Theta^*) = \hat{u}_i + \Theta^* (\hat{u}_j - \hat{u}_i). \quad (42)$$

References

- Agianniotis, A., Rachev, A., and Stergiopoulos, N. (2012). Active axial stress in mouse aorta. *Journal of Biomechanics*, 45(11):1924–1927.
- Ancombe, F. J. (1973). Graphs in statistical analysis. *The American Statistician*, 27:17–21.
- Badel, P., Avril, S., Lessner, S., and Sutton, M. (2012). Mechanical identification of layer-specific properties of mouse carotid arteries using 3D-DIC and a hyperelastic anisotropic constitutive model. *Computer Methods in Biomechanics and Biomedical Engineering*, 15:37–48.
- Balzani, D., Neff, P., Schröder, J., and Holzapfel, G. A. (2006). A polyconvex framework for soft biological tissues. adjustment to experimental data. *International Journal of Solids and Structures*, 43:6052–6070.
- Böl, M., Schmitz, A., Nowak, G., and Siebert, T. (2012). A three-dimensional chemo-mechanical continuum model for smooth muscle contraction. *Journal of the Mechanical Behavior of Biomedical Materials*, 13:215–229.
- Butenko, S. and Pardalos, P. M. (2014). *Numerical Methods and Optimization: An Introduction*. Taylor & Francis.
- Cardoso, L., Kelly-Arnold, A., Maldonado, N., Laudier, D., and Weinbaum, S. (2014). Effect of tissue properties, shape and orientation of microcalcifications on vulnerable cap stability using different hyperelastic constitutive models. *Journal of Biomechanics*, 47:870–877.
- Chen, H., Luo, T., Zhao, X., Lu, X., Huo, Y., and Kassab, G. S. (2013). Microstructural constitutive model of active coronary media. *Biomaterials*, 34:7575–7583.
- Chuong, C. J. and Fung, Y. C. (1983). Three-dimensional stress distribution in arteries. *Journal of Biomechanical Engineering*, 105:268–274.
- Criscione, J. C., Sacks, M. S., and Hunter, W. C. (2003a). Experimentally tractable, pseudo-elastic constitutive law for biomembranes: I. theory. *Journal of Biomechanical Engineering*, 125:94–99.
- Criscione, J. C., Sacks, M. S., and Hunter, W. C. (2003b). Experimentally tractable, pseudo-elastic constitutive law for biomembranes: II. application. *Journal of Biomechanical Engineering*, 125:100–105.
- Daniels, R. W. (1978). *Introduction to Numerical Methods and Optimization Techniques*. Elsevier Science Ltd.
- Delfino, A., Stergiopoulos, N., Moore, J. E., and Meister, J.-J. (1997). Residual strain effects on the stress field in a thick wall finite element model of the human carotid bifurcation. *Journal of Biomechanics*, 30:777–786.
- Deng, S. X., Tomioka, J., Debes, J. C., and Fung, Y. C. (1994). New experiments on shear modulus of elasticity of arteries. *The American Journal of Physiology*, 266:1–10.
- Dennis, J. E. and Schnabel, R. B. (1996). *Numerical Methods for Unconstrained Optimization and Nonlinear Equations*. Society for Industrial and Applied Mathematics.
- Draper, N. R. and Smith, H. (1998). *Applied Regression Analysis*. John Wiley & Sons, Inc.
- Dumoulin, C. and Cochelin, B. (2000). Mechanical behaviour modelling of balloon-expandable stents. *Journal of Biomechanics*, 33:1461–1470.
- Fung, Y. C., Fronek, K., and Patitucci, P. (1979). Pseudoelasticity of arteries and of its mathematical expression. *American Physiological Society*, 237:H620–H631.
- Gasser, T. C. and Holzapfel, G. A. (2002). A rate-independent elastoplastic constitutive model for biological fiber-reinforced composites at finite strains: continuum basis, algorithmic formulation and finite element implementation. *Computational Mechanics*, 29:340–360.
- Gasser, T. C. and Holzapfel, G. A. (2007). Modeling plaque fissuring and dissection during balloon angioplasty intervention. *Annals of Biomedical Engineering*, 35:711–723.
- Gasser, T. C., Ogden, R. W., and Holzapfel, G. A. (2006). Hyperelastic modelling of arterial layers with distributed collagen fibre orientations. *Journal of the Royal Society, Interface*, 3(6):15–35.
- GiD-Manual (2012). *GiD: Reference Manual*. GiD.
- Gleason, R. L., Dye, W. W., Wilson, E., and Humphrey, J. D. (2008). Quantification of the mechanical behavior of carotid arteries from wild-type, dystrophin-deficient, and sarcoglycan-delta knockout mice. *Journal of Biomechanics*, 41:3213–3218.
- Gourisankaran, V. and Sharma, M. G. (2000). The finite element analysis of stresses in atherosclerotic arteries during balloon angioplasty. *Critical Reviews in Biomedical Engineering*, 28:47–51.
- Guccione, J. M., McCulloch, A. D., and Waldman, L. K. (1991). Passive material properties of intact ventricular myocardium determined from a cylindrical model. *Journal of Biomechanical Engineering*, 113:42–55.
- Hartmann, S. and Neff, P. (2003). Polyconvexity of generalized polynomial-type hyperelastic strain energy functions for near-incompressibility. *International Journal of Solids and Structures*, 40:2767–2791.
- Hartmann, S. and Sguzzo, C. (2015). Strain analysis in sandwich structures using digital image correlation. *Werkstoffeigenschaften und -verhalten*, 2:61–71.
- Hartmann, S., Tschöpe, T., Schreiber, L., and Haupt, P. (2003). Finite deformations of a carbon black-filled rubber.

- experiment, optical measurement and material parameter identification using finite elements. *European Journal of Mechanics - A/Solids*, 22:309–324.
- Haupt, P. (2001). *Continuum Mechanics and Theory of Materials*. Springer.
- Hollander, Y., Durban, D., Lu, X., Kassab, G. S., and Lanir, Y. (2011). Constitutive modeling of coronary arterial media—comparison of three model classes. *Journal of Biomechanical Engineering*, 133:061008–061020.
- Holzapfel, G. A., Gasser, T. C., and Ogden, R. W. (2000). A new constitutive framework for arterial wall mechanics and a comparative study of material models. *Journal of Elasticity*, 61:1–48.
- Holzapfel, G. A., Gasser, T. C., and Stadler, M. (2002). A structural model for the viscoelastic behavior of arterial walls: Continuum formulation and finite element analysis. *European Journal of Mechanics - A/Solids*, 21:441–463.
- Holzapfel, G. A., Niestrawska, J. A., Ogden, R. W., Reinisch, A. J., and Schriefl, A. J. (2015). Modelling non-symmetric collagen fibre dispersion in arterial walls. *Journal of the Royal Society, Interface / the Royal Society*, 12(106).
- Holzapfel, G. A., Sommer, G., Gasser, C. T., and Regitnig, P. (2005). Determination of layer-specific mechanical properties of human coronary arteries with nonatherosclerotic intimal thickening and related constitutive modeling. *American Journal of Physiology*, 289:H2048–H2058.
- Iannaccone, F., Debusschere, N., De Bock, S., De Beule, M., Van Loo, D., Vermassen, F., Segers, P., and Verheghe, B. (2014). The influence of vascular anatomy on carotid artery stenting: a parametric study for damage assessment. *Journal of Biomechanics*, 47:890–898.
- Itskov, M., Ehret, A. E., and Mavrilas, D. (2006). A polyconvex anisotropic strain-energy function for soft collagenous tissues. *Biomechanics and modeling in mechanobiology*, 5:17–26.
- Krämer, S., Rothe, S., and Hartmann, S. (2015). Homogeneous stress–strain states computed by 3D-stress algorithms of fe-codes: application to material parameter identification. *Engineering with Computers*, 31:141–159.
- Kreißig, R. (1998). *Auswertung inhomogener Verschiebungsfelder zur Identifikation der Parameter elastisch-plastischer Deformationsgesetze*. *Forschung im Ingenieurwesen*, 64:99–109.
- L'italien, G. J., Chandrasekar, N. R., Lamuraglia, G. M., Pevec, W. C., Dhara, S., Warnock, D. F., and Abbott, W. M. (1994). Biaxial elastic properties of rat arteries in vivo: influence of vascular wall cells on anisotropy. *American Journal of Physiology - Heart and Circulatory Physiology*, 267:H574–H579.
- Lu, S.-H., Sacks, M. S., Chung, S. Y., Gloeckner, D. C., Pruchnic, R., Huard, J., de Groat, W. C., and Chancellor, M. B. (2005). Biaxial mechanical properties of muscle-derived cell seeded small intestinal submucosa for bladder wall reconstitution. *Biomaterials*, 26:443–449.
- Mahnken, R. and Stein, E. (1996). A unified approach for parameter identification of inelastic material models in the frame of the finite element method. *Computer Methods in Applied Mechanics and Engineering*, 136:225–258.
- Ning, J., Xu, S., Wang, Y., Lessner, S. M., Sutton, M. A., Anderson, K., and Bischoff, J. E. (2010). Deformation measurements and material property estimation of mouse carotid artery using a microstructure-based constitutive model. *Journal of Biomechanical Engineering*, 132:121010–121023.
- Nocedal, J. and Wright, S. J. (2006). *Numerical Optimization*. Springer.
- Nolan, D. R., Gower, A. L., Destrade, M., Ogden, R. W., and McGarry, J. P. (2014). A robust anisotropic hyperelastic formulation for the modelling of soft tissue. *Journal of the Mechanical Behavior of Biomedical Materials*, 39:48–60.
- Okamoto, R. J., Wagenseil, J. E., DeLong, W. R., Peterson, S. J., Kouchoukos, N. T., and Sund, I. (2002). Mechanical properties of dilated human ascending aorta. *Annals of Biomedical Engineering*, 30:624–635.
- Otsuka, F., Yahagi, K., Sakakura, K., and Virmani, R. (2013). Why is the mammary artery so special and what protects it from atherosclerosis? *Annals of Cardiothoracic Surgery*, 2(4):519–526.
- Ottensmeyer, M. P., Kerdok, A. E., Howe, R. D., and Dawson, S. L. (2004). The effects of testing environment on the viscoelastic properties of soft tissues. *Proceedings of Medical Simulation: International Symposium - ISMS 2004*, 3078:9–18.
- Rhodin, J. A. G. (2011). Architecture of the vessel wall. *Comprehensive Physiology*, pages 1–31.
- Rivlin, R. S. and Saunders, D. W. (1951). Large elastic deformations of isotropic materials. vii. experiments on the deformation of rubber. *Philosophical Transactions of the Royal Society of London. Series A*, 243:251–288.
- Sacks, M. S. (2000). Biaxial mechanical evaluation of planar biological materials. *Journal of Elasticity*, 61:199–246.
- Scheday, G. (2003). *Theorie und Numerik der Parameteridentifikation von Materialmodellen der finiten Elastizität und Inelastizität auf der Grundlage optischer Feldmessmethoden*. PhD thesis, University of Stuttgart.
- Schmitz, A. and Böhl, M. (2011). On a phenomenological model for active smooth muscle contraction. *Journal of*

- Biomechanics*, 44:2090–2095.
- Schröder, J. and Neff, P. (2001). On the construction of polyconvex anisotropic free energy functions. *Proceedings of the IUTAM Symposium on Computational Mechanics of Solid Materials at Large Strains*, 108:171–180.
- Schröder, J. and Neff, P. (2002). Application of polyconvex anisotropic free energies to soft tissues. *Fifth World Congress on Computational Mechanics*.
- Schröder, J. and Neff, P. (2003). Invariant formulation of hyperelastic transverse isotropy based on polyconvex free energy functions. *International Journal of Solids and Structures*, 40:401–445.
- Stålhand, J., Klarbring, A., and Holzapfel, G. A. (2011). A mechanochemical 3D continuum model for smooth muscle contraction under finite strains. *Journal of Theoretical Biology*, 268:120–130.
- Sun, W., Sacks, M. S., and Scott, M. J. (2003). Numerical simulations of the planar biaxial mechanical behavior of biological materials. *ASME Summer Bioengineering Conference, Miami, FL*.
- Sutton, M. A., Ke, X., Lessner, S. M., Goldbach, M., Yost, M., Zhao, F., and Schreier, H. W. (2008). Strain field measurements on mouse carotid arteries using microscopic three-dimensional digital image correlation. *Journal of Biomedical Materials Research*, 84:178–190.
- Suzuki, S. and Abe, K. (1985). Topological structural analysis of digitized binary images by border following. *Computer Vision, Graphics, and Image Processing*, 30(1):32–46.
- Takamizawa, K. and Hayashi, K. (1987). Strain energy density function and uniform strain hypothesis for arterial mechanics. *Journal of Biomechanics*, 20:7–17.
- Vaishnav, R. N., Young, J. T., and Patel, D. J. (1973). Distribution of stresses and of strain-energy density through the wall thickness in a canine aortic segment. *Circulation Research*, 32:577–583.
- Virues Delgadillo, J. O., Delorme, S., Diraddo, R., Hatzikiriakos, S. G., and Thibault, F. (2006). Mechanical characterization of arterial wall : Should cruciform or square sample be used in biaxial testing? *Journal of Biomechanical Engineering*.
- von Maltzahn, W. W., Warriyar, R. G., and Keitzer, W. F. (1984). Experimental measurements of elastic properties of media and adventitia of bovine carotid arteries. *Journal of Biomechanics*, 17:839–847.
- Weiss, J. A., Maker, B. N., and Govindjee, S. (1996). Finite element implementation of incompressible, transversely isotropic hyperelasticity. *Computer Methods in Applied Mechanics and Engineering*, 135:107–128.
- Wu, W., Qi, M., Liu, X.-P., Yang, D.-Z., and Wang, W.-Q. (2007). Delivery and release of nitinol stent in carotid artery and their interactions: a finite element analysis. *Journal of Biomechanics*, 40:3034–3040.
- Xie, J., Zhou, J., and Fung, Y. C. (1995). Bending of blood vessel wall: stress-strain laws of the intima-media and adventitial layers. *Journal of Biomechanical Engineering*, 117:136–145.
- Yosibash, Z., Manor, I., Gilad, I., and Willentz, U. (2014). Experimental evidence of the compressibility of arteries. *Journal of the Mechanical Behavior of Biomedical Materials*, 39:339–354.
- Yosibash, Z. and Priel, E. (2012). Artery active mechanical response: High order finite element implementation and investigation. *Computer Methods in Applied Mechanics and Engineering*, 237-240:51–66.
- Yu, Q., Zhou, J., and Fung, Y. C. (1993). Neutral axis location in bending and young’s modulus of different layers of arterial wall. *American Physiological Society*, 265(1 Pt 2):H52–H60.
- Zdunek, A., Rachowicz, W., and Eriksson, T. (2014). A novel computational formulation for nearly incompressible and nearly inextensible finite hyperelasticity. *Computer Methods in Applied Mechanics and Engineering*, 281:220–249.